Available online at www.sciencedirect.com
ScienceDirect
Tectonophysics 441 (2007) 1–26
TECTONOPHYSICS
www.elsevier.com/locate/tecto

Transfer zones and fault reactivation in inverted rift basins: Insights from physical modelling

Elena A. Konstantinovskaya *, Lyal B. Harris, Jimmy Poulin, Gennady M. Ivanov

Institut National de la Recherche Scientifique, Centre Eau, Terre et Environnement (INRS-ETE), 490 rue de la Couronne, Quebec City, Quebec, Canada G1K 9A9

Received 14 November 2006; received in revised form 9 May 2007; accepted 3 June 2007
Available online 21 June 2007

Abstract

Lateral transfer zones of deformation and fault reactivation were investigated in multilayered silicone–sand models during extension and subsequent co-axial shortening. Model materials were selected to meet similarity criteria and to be distinguished on CT scans; this approach permitted non-destructive visualisation of the progressive evolution of structures. Transfer zones were initiated by an orthogonal offset in the geometry of a basal mobile aluminium sheet and/or by variations of layer thickness or material rheology in basal layers. Transfer zones affected rift propagation and fault kinematics in models. Propagation and overlapping rift culminations occurred in transfer zones during extension. During shortening, deviation in the orientation of frontal thrusts and fold axes occurred within transfer zones in brittle and ductile layers, respectively. CT scans showed that steep (58–67°) rift-margin normal faults were reactivated as reverse faults. The reactivated faults rotated to shallower dips (19–38°) with continuing shortening after 100% inversion. Rotation of rift phase faults appears to be due to deep level folding and uplift during the inversion phase. New thrust faults with shallow dips (20–34°) formed outside the inverted graben at late stages of shortening. Frontal ramps propagated laterally past the transfer structure during shortening. During inversion, the layers filling the rift structures underwent lateral compression at the depth, the graben fill was pushed up and outwards creating local extension near the surface. Sand marker layers in inverted graben have showed fold-like structures or rotation and tilting in the rifts and on the rift margins. The results of our experiments conform well to natural examples of inverted graben. Inverted rift basins are structurally complex and often difficult to interpret in seismic data. The models may help to unravel the structure and evolution of these systems, leading to improved hydrocarbon exploration assessments. Model results may also be used to help predict the location of basement discontinuities which may have focused hydrothermal fluids during basin formation and inversion.

Keywords: Physical modelling; CT scans; Transfer zones; Fault reactivation; Inversion; Rifting

1. Introduction

1.1. Transfer zones and basement discontinuities

Transfer zones may play an important role during rifting and subsequent basin inversion. Discrete basement faults influence the localisation and orientation of

* Corresponding author. Tel.: +1 418 654 2559; fax: +1 418 654 2600.
E-mail address: ekonst@sympatico.ca (E.A. Konstantinovskaya).

0040-1951/$ - see front matter © 2007 Elsevier B.V. All rights reserved.
doi:10.1016/j.tecto.2007.06.002

normal faults and transfer zones developed during rifting in sedimentary basins (Morley et al., 1990; Byrne and Harris, 1992; Doré et al., 1997; Tavarnelli et al., 2004; Wilson et al., 2006). Transfer zones formed during rifting affect the evolution of subsequent compressional structures during basin inversion (Etheridge, 1986). For example, a synrift accommodation zone comprising a relay ramp or transfer fault orthogonal to the basin margin likely controlled the formation of superimposed folds during inversion of the Mesozoic Atlas paleorift (Beauchamp, 2004). Variations in basement rheology may also exert primary controls on basin-scale fault localisation and spacing, and influence depositional and reactivation histories (Harris et al., 1994; O'Brien et al., 1996, 1999; Paton and Underhill, 2004).

Previous sandbox modelling studies have shown that basement discontinuities exert a significant influence on the geometry and orientation of transfer zones during rifting in sedimentary basins (Acocella et al., 1999; Le Calvez and Vendeville, 2002; Gartrell et al., 2005). Contacts between basement blocks of different rheologies in analogue models of Harris et al. (1994), O'Brien et al. (1996, 1999) and Higgins and Harris (1997) controlled the orientation and spacing of faults and the localisation of sub-basins in overlying sand layers. Vertical basement offsets or the horizontal offsets of a backstop induced deformation in transfer zones in sandbox thrust wedges (Calassou et al., 1993). Frontal thrust faults in the wedges propagated synchronously or alternatively, anastomosing as oblique ramps within the transfer zones. The evolution of transfer zones was tested in sand–silicone models constructed with a pre-existing basement fault located between two laterally offset rift basins (Gartrell et al., 2005). The formation of a series of *en relais* normal faults was observed in the transfer zones during the extensional phase. Both the rift faults and the basement fault were reactivated and a cross-trending wrench fault developed in the transfer zone during the oblique inversion phase in these models.

The significant improvement that the CT scanning brings is the ability to see the cross-sectional structural evolution of the model through both the extension and inversion phases. In the models of Gartrell et al. (2005), it was only possible to observe cross-sections at the completion of the experiments. The X-ray computed tomography ("CT-scanning") approach previously applied with success in analogue modelling (e.g. Schreurs et al., 2003; Panien et al., 2005) enabled us to visualise for the first time fault reactivation and 3D deformation in transfer zones formed in silicone–sand models continuously during extension and co-axial inversion stages.

1.2. Reactivation of normal faults during basin inversion

Reverse reactivation of normal faults during basin inversion is reported from many fold–thrust belts (Chandler et al., 1989; Withjack et al., 1995; Beauchamp et al., 1996, 1999; Gomez et al., 2000; Hill et al., 2004). Inversion of normal faults depends on their initial geometry and orientation with respect to the direction of contraction (Etheridge, 1986; McClay, 1989; Holdsworth et al., 1997; Walsh et al., 2001). Theoretical analyses of fault reactivation (Etheridge, 1986) show that the contrast in cohesive and frictional strengths between intact and previously faulted rocks is one of the principal parameters controlling fault reactivation. Differences in whether faults are reactivated or not have been obtained in previous analogue modelling studies. Inversion of normal faults was obtained for hanging-wall sand models deformed above rigid detachments (Cooke and Harris, 1987; Buchanan and McClay, 1991; Yamada and McClay, 2004), for clay models (Eisenstadt and Withjack, 1995), and for sand models deformed above silicone layers (Gartrell et al., 2005). Inversion of normal faults was also obtained in cohesive models of a wet sand–cement mixture above viscous putty (Mandal and Chattopadhyay, 1995). Eisenstadt and Withjack (1995) reported that normal faults are reverse reactivated in clay models with up to 50% inversion, while new flatter thrusts accommodate shortening after 100% to 200% inversion. Panien et al. (2005) noted that new thrusts cut off pre-existing normal faults during graben inversion in layered sand models with no significant normal fault reactivation. Dubois et al. (2002) showed that all older faults were reactivated in sand–silicone experiments without sedimentation, whereas some of the older faults were not reactivated in experiments with sedimentation.

Mandl (2000) showed that in cohesionless or cohesive rocks under horizontal extension, the hanging wall can easily slide down a *steep* plane of weakness, but much less easily on a low-angle plane. In contrast, horizontal contraction can push the hanging wall up a low-angle plane, but reverse movement of the hanging wall on a *steep* plane of weakness is more difficult, and requires exceptional lubrification of the steep plane, or a moderate to strong cohesion of the intact rock to suppress the formation of new thrust faults. Hence, Mandl (2000) concluded that reverse reactivation of *steep* faults cannot be simulated by *horizontal* shortening in model experiments with dry sand. However, reverse reactivation of *steep* normal faults was produced experimentally in sand models (Koopman et al., 1987) and in silicone–sand models (Gartrell et al., 2005). In

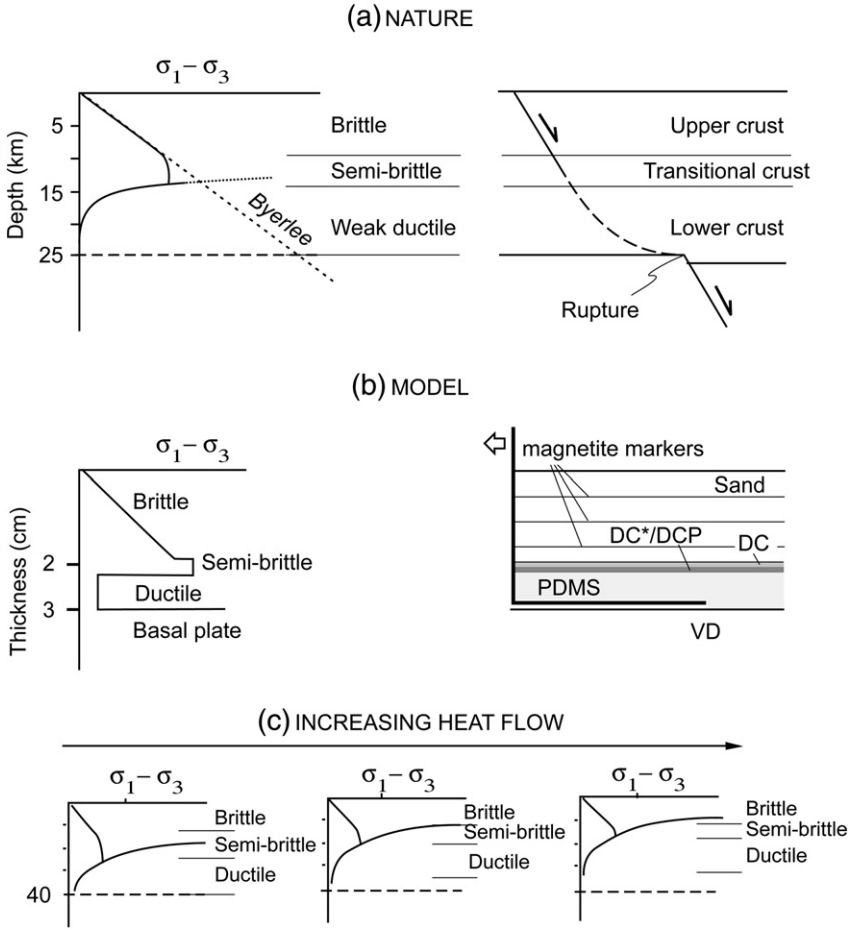

Fig. 1. Strength profiles. (a) Strength profile for a continental crust with a geothermal gradient of 20 °C km^{-1} and a shear strain rate of 10^{-12} s^{-1}, after Ord and Hobbs (1989). The Byerlee (1968) relationship breaks down at about 10 km, and below this depth, shear resistance is independent of the normal stress. Transitional zones in the middle crust show a non-linear increase in strength with depth and semi-brittle behaviour. (b) Strength profile for experiments. Sand was used to simulate the brittle parts of the crust while silicone putty±modelling clay (see Table 1) was used to imitate the semi-brittle behaviour of the middle crust and PDMS simulates the ductile behaviour of the lower crust. (c) Effect of increasing heat flow on the distribution of rheological layers in a simple crustal system, after Gartrell (2001). The middle crustal (semi-brittle) layer diminishes in thickness with increasing heat flow, whereas the thickness of upper and lower crustal layers remains relatively unchanged.

the models of Koopman et al. (1987), steep (60°) normal faults formed at graben boundaries as the direct result of the *subsidence* of a competent basement block were reactivated as reverse faults by *upward movement* of the block driven by the inward movement of confining blocks. In the models of Gartrell et al. (2005), steep normal faults bounded the rift basins as a result of necking of the strong putty layer were reactivated due to folding and buckling in the silicone layer.

In our study, reverse reactivation of normal faults was investigated using dry sand layers overlying a ductile silicone base in three-layer models under horizontal extension and co-axial shortening. Homogeneous material was used for pre-rift and synrift sand layers. Deformation of models was studied through cross-sections and 3D reconstructions based on successive CT scans and physical slices of final models. CT-scanning enabled the visualisation as to whether *steep* faults formed in sand layers during extension are reactivated

Table 1
Composition of mixtures of high viscosity putty Dow Corning 3179 Dilatant Compound (DC) with strontium aluminate powder (DC*) and modelling putty (DCP1, DCP2) used in the experiments

Ductile layer	Dow Corning 3179 Dilatant Compound, %	Strontium aluminate powder, %	Modelling putty, %	Densities, g/cm^3
DC	100	–	–	1.14
DC*	92	8	–	1.23
DCP1	80	4	16	1.28
DCP2	56	–	44	1.42

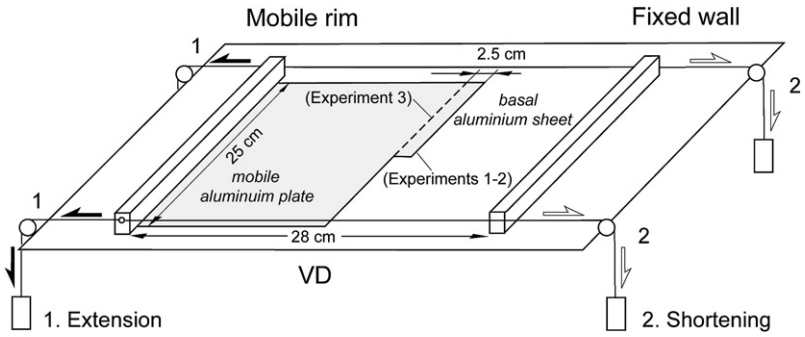

Fig. 2. Experimental apparatus. A thin mobile aluminium plate was attached to a moving wall. The edge of the mobile plate induced a velocity discontinuity (VD) in models. Tractional forces were asymmetric, with only one half of the model being extended. Arrows indicate the directions for stages of extension and subsequent co-axial shortening.

along the *same fault planes* during subsequent shortening in the same model or whether new faults are developed. The quantitative analysis of lateral compression was made for deep levels of inverted graben structures and for synrift fill deformed during shortening stages. The initial data for the beginning of shortening were taken for the *last* stage of extension visualised on CT scans. A study of subsequent stages of deformation of the models by CT images allowed us to quantify if the lateral compression of graben fill was observed during graben inversion and how it was distributed with depth.

2. Materials and methods

2.1. Scaling and modelling materials

Analogue modelling of crustal deformation is geometrically, kinematically and dynamically similar to that

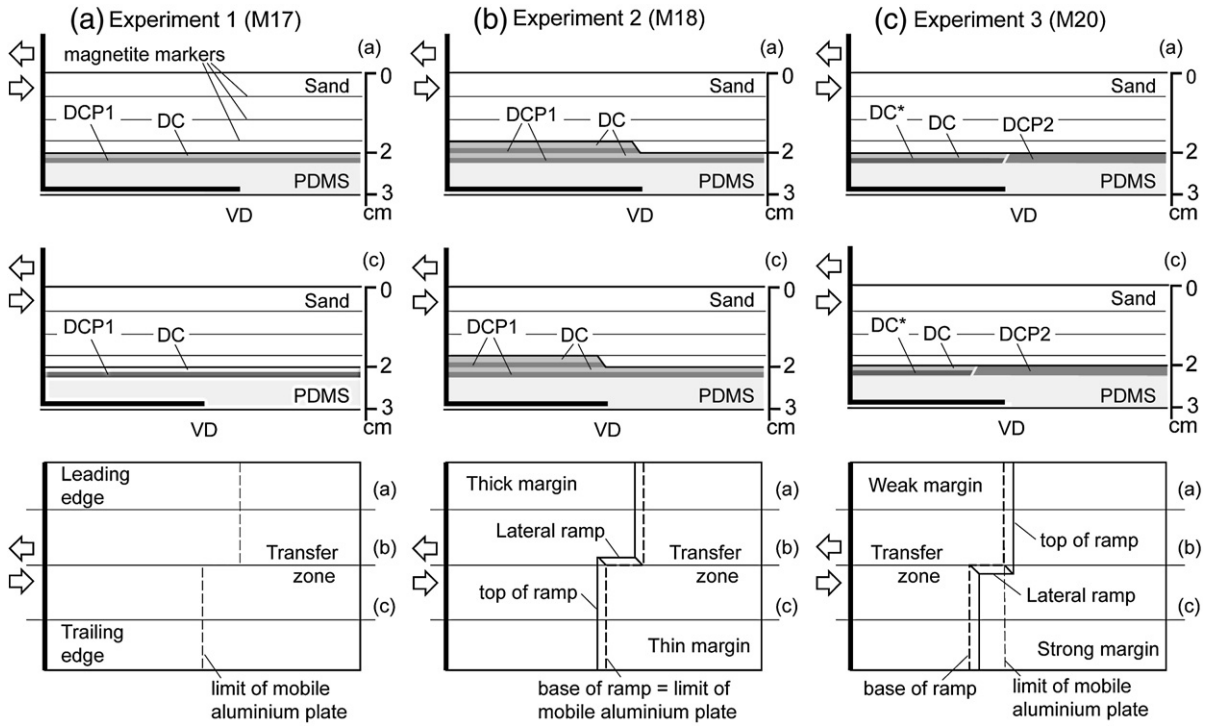

Fig. 3. Schematic representation of multilayered silicone–sand models before deformation. The locations of cross-sections across leading and trailing edges of models are shown in plan views. The thicknesses and rheology of layers varied for different models (see text and Table 1 for the ductile layer composition). Magnetite sand layers serve as markers on CT scans. Note that the geometry of the mobile aluminium plate is similar to (Experiment 2) and differs from (Experiment 3) the shape of the basal ramp in the strong ductile layer. VD = velocity discontinuity.

in nature if experimental models and natural systems are characterised by a similar distribution of stress, densities, and rheologies (Hubbert, 1937; Ramberg, 1981). Continental lithosphere is rheologically stratified, reflecting changes with depth in mechanical behaviour and flow process (Kirby, 1983; Ord and Hobbs, 1989). Rheological strength profiles thus provide a guide for modelling the mechanical behaviour of the lithosphere. The brittle fracture of most rocks in the upper crust is assumed to be proportional to depth, according to the Byerlee law (Byerlee, 1968). Ductile creep deformation of rocks in the lower crust is assumed to be described by a power law (Kirby, 1983). However, as assumed by Ord and Hobbs (1989), the Byerlee relationship probably breaks down at moderate depths (10–15 km) due to increase in confining pressure. Transitional zones in the middle crust show a non-linear increase in strength with depth and semi-brittle behaviour (Fig. 1a).

The choice of materials and scaling factors for the simplified two-layered models using sand and silicone putty was explained in previous studies (e.g. Davy and Cobbold, 1991; Brun and Nalpas, 1996; Michon and Sokoutis, 2005). Three-layered models were tested by Gartrell (1997, 2001; Gartrell et al., 2005). In these models, sand was used for the upper crust and two types of silicone putty for the semi-brittle middle crust and for the weak ductile lower crust. In our models, similar three-layered models with a semi-brittle transition zone were used (Fig. 1b). The length and thickness scaling

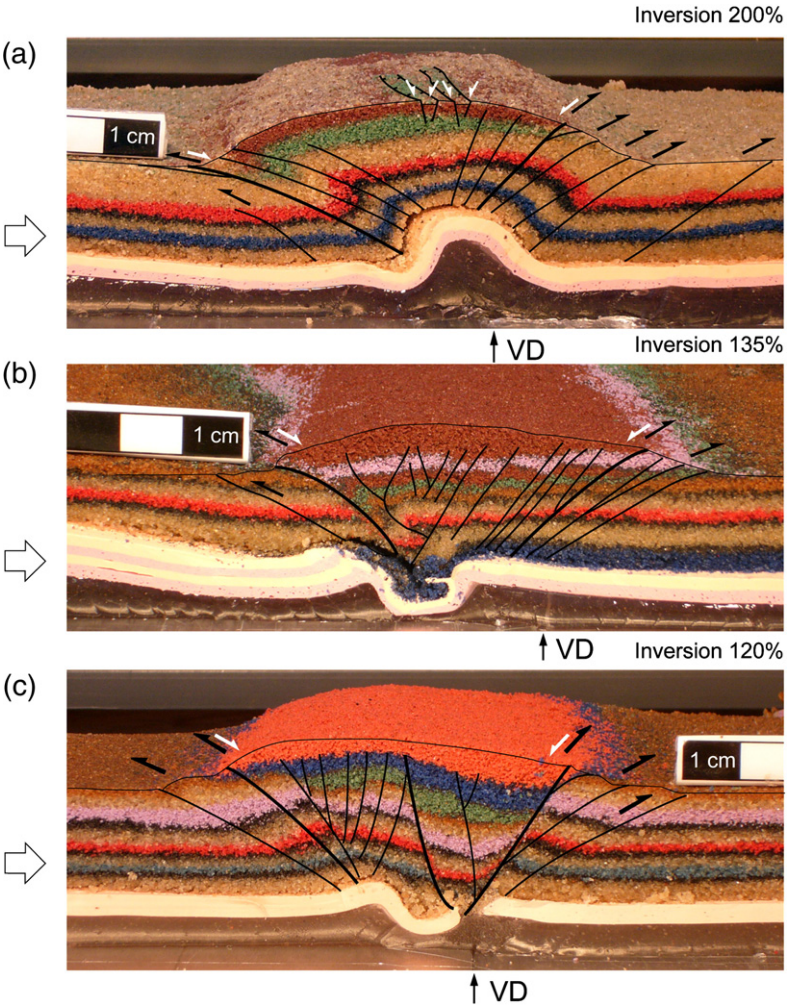

Fig. 4. Experiments 1–3. Photographs of cross-sections across the leading parts of models 17 (a), 18 (b), and 20 (c) at the end of shortening. Location of the cross-sections corresponds to lines (a) in Fig. 3. Experiment 1, 200% inversion (25 mm extension, 50 mm shortening), Experiment 2, 135% inversion (37 mm extension, 50 mm shortening), Experiment 3, 120% inversion (25 mm extension, 30 mm shortening). VD = velocity discontinuity.

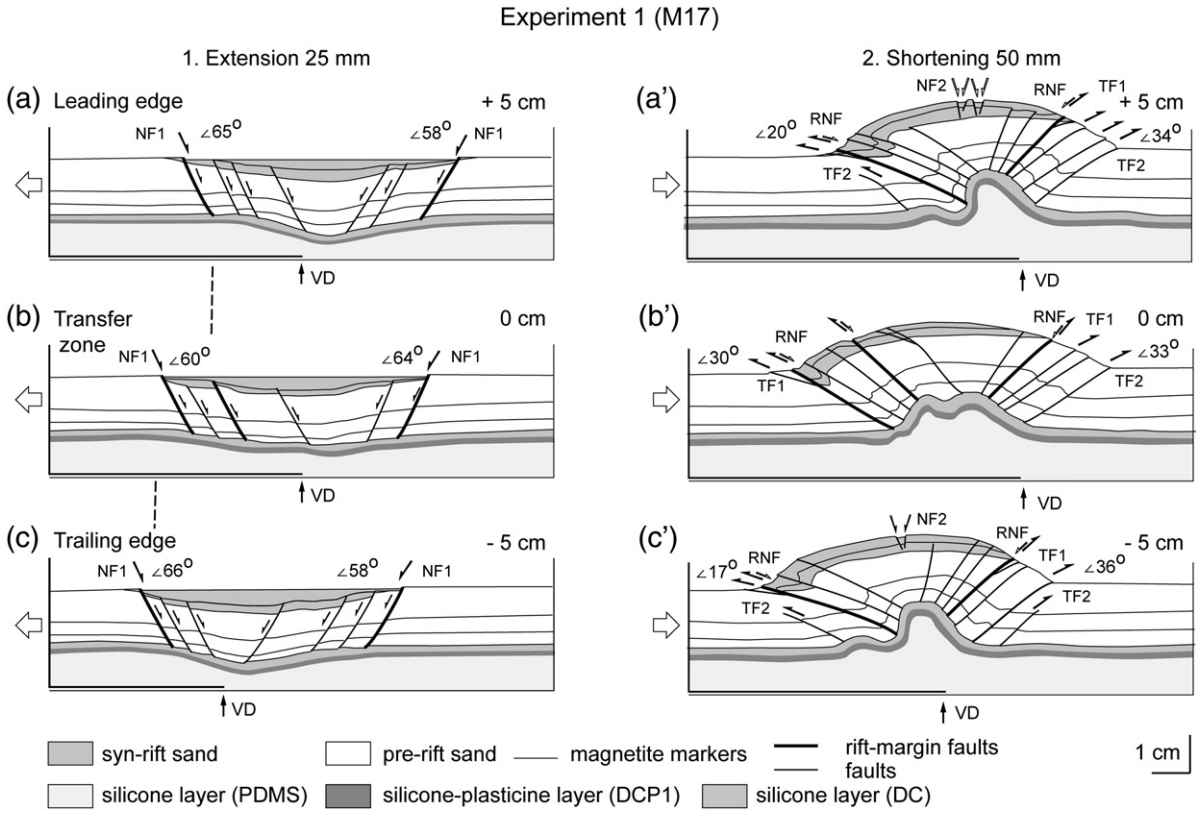

Fig. 5. Experiment 1. Drawings from X-ray CT images of scan cross-sections for model 17 at the end of extension (a–c) and at the end of shortening (a′–c′). The location of the cross-sections is shown in Fig. 3a. Boudinage and folding occurred in the lower ductile layers during extension and shortening respectively, while mostly faulting was produced at the upper brittle layer. The graben and inversion structures were symmetric. The thickness of synrift sand layers was less along the central cross-section in comparison to the edges of the model. NF = normal faults; RNF = reverse reactivated normal faults; TF = thrust faults; VD = velocity discontinuity.

factor was such that 2 cm in the model (thickness of the sand layers representing brittle crust) equated to 10 to 15 km in nature (range in average depth to the upper brittle–ductile transition in continental crust, Sonder and England, 1986). Model materials were selected to meet similarity criteria and to be distinguished on CT scans; this approach permitted non-destructive visualisation of the progressive evolution of structures. Models were composed of 1) an upper brittle layer of dry quartz sand with magnetite sand marker layers (upper crust); 2) a strong ductile multilayer comprising high viscosity silicone putty (middle crust); 3) a ductile layer of low viscosity silicone putty (lower crust) (Fig. 1b). The admixtures of a strontium aluminate–europium powder and/or of a modelling putty (Table 1) in the strong ductile multilayer helped visualisation of deformation in ductile layers on CT scans. The strong ductile multilayer was thin, and the strength profile of models corresponded to the regions with relatively high geothermal gradient (Fig. 1c; Gartrell, 2001).

The physical characteristics of the materials used are as follows:

(1) The dry aeolian quartz sand, sieved to 0.5–0.25 mm, is a Mohr–Coulomb material with a 30° angle of internal friction, no cohesion, and a bulk density ρ of 1.64 g/cm^3. Alternating coloured sand layers 0.5 cm-thick are used in the models. Magnetite layers 1 mm-thick were sieved at the base of each coloured sand layer to distinguish layering in CT scans. The total thickness of the sand layers was 2 cm.

(2) The higher viscosity silicone putty (Dow Corning 3179 Dilatant Compound, DC) has a viscosity of 4×10^5 Pa s at 23 °C at the strain rate of the experiment and acts as a Newtonian fluid. A 3 mm-thick multilayer was used in the experiments consisting of alternating thin layers of DC silicone and its mixture with a strontium aluminate–europium powder DC* (Ultra Green Glow in the Dark Powder™ from Glow

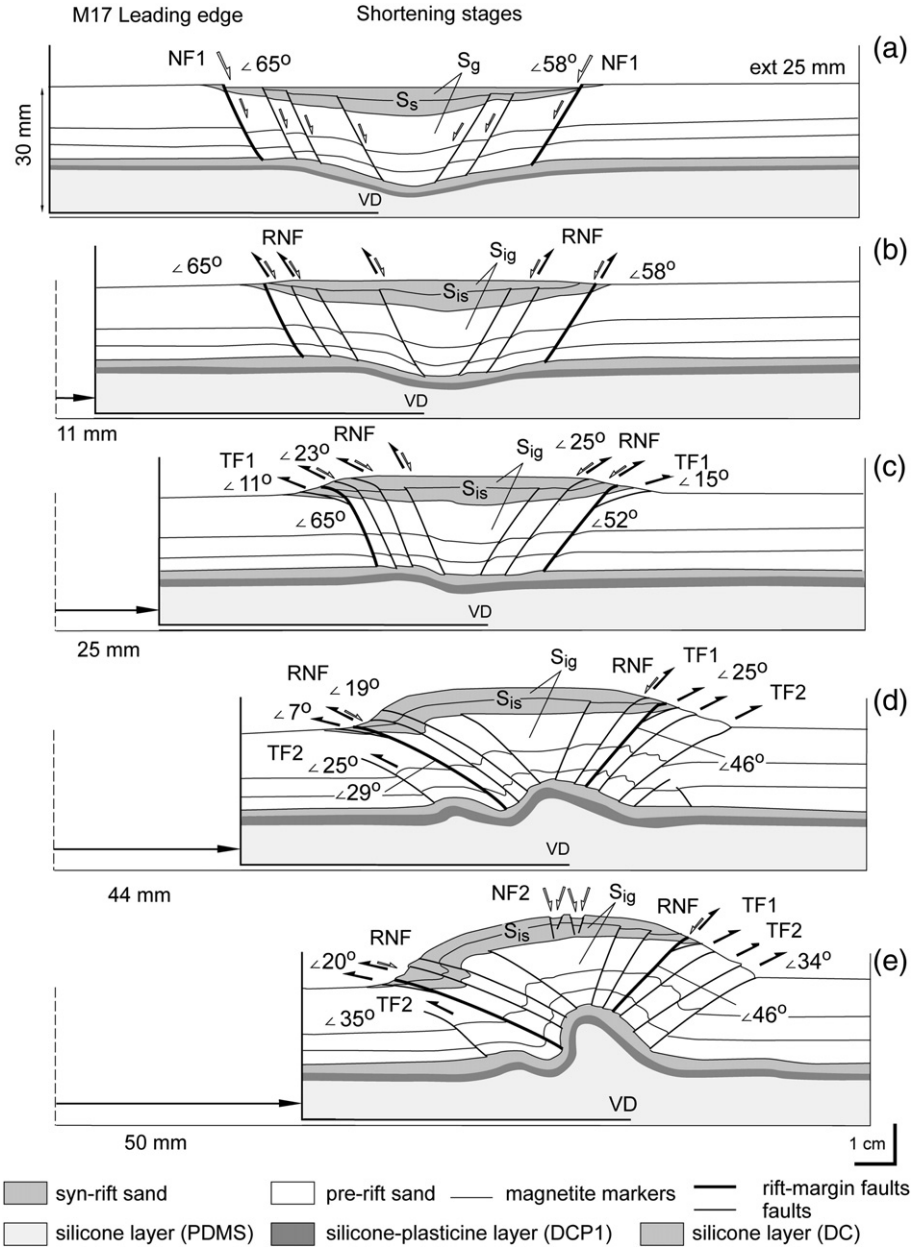

Fig. 6. Experiment 1. Drawings from X-ray CT images of scan sections across the leading part of model 17 obtained for subsequent stages of shortening. Location of the cross-section is shown in Figs. 3a and 7 (profile a). The steep-bounding normal faults were reverse reactivated (RNF) (b–c). After 100% inversion, RNF progressively rotated and flattened (c–e) followed by subsequent formation of flatter thrust faults TF1–TF2 outside of the original graben boundaries (c–e). Note late extensional faults at the top of the inversion structure (NF2) after 200% inversion. VD = velocity discontinuity.

Inc.) and/or with a modelling putty (similar to plasticine) DCP1 and DCP2 (Table 1) which provide marker layers discernible on CT scans (Poulin et al., 2006).

(3) The lower viscosity silicone putty polydimethylsiloxane (PDMS) has a density of 0.98 g/cm^3, its viscosity is 3×10^4 Pa s at 23 °C and it responds to slow strain as a Newtonian fluid. A 7 mm-thick layer of PDMS was used in the experiments.

2.2. Model set-up and experimental procedure

The two-layered silicone and sand models were built in a wooden sandbox comprising a fixed wall and a moving wall (Fig. 2). Models were consequently deformed during extension and shortening phases by moving one of the vertical sandbox walls. A thin mobile aluminium plate was attached to the moving wall and it was pulled or pushed

during experiments by a system of pulleys and weights. The rigid basal wooden plate was covered by a thin aluminium sheet. The limit of the moving aluminium plate created a velocity discontinuity (VD) at the base of the model that helped to localise deformation. The moving plate had an orthogonal offset (in plan view) in Experiments 1–2, and it was linear in Experiment 3 (Fig. 2). Transfer zones were initiated by an orthogonal offset in the basal plate or in the boundary between ductile layers of different rheologies (Fig. 3).

As extension proceeded and rift basins developed, further sand layers with magnetite markers were added to structural depressions to simulate synrift sedimentation. After 2.5–3.7 cm extension, subsequent shortening was achieved by driving the moving wall toward the centre of the model. A series of lateral sections at 1 cm intervals across models was obtained through CT-scanning for each 0.6–1.5 cm of extension or shortening using a third-generation sliding gantry Siemens Somatom Volume Access medical CT scanner in the Multidisciplinary Scanning Laboratory at INRS-ETE. On completion of experiments, the models were cut in section at the same 1 cm intervals.

3. Results

3.1. Experiment 1 (M17)

This model comprised sand and silicone layers of equal thickness and constant compositions across the model (Figs. 3a and 4a). The basal mobile plate had an orthogonal offset in plan view. At the beginning of extension, thinning and shearing of ductile layers occurred above the

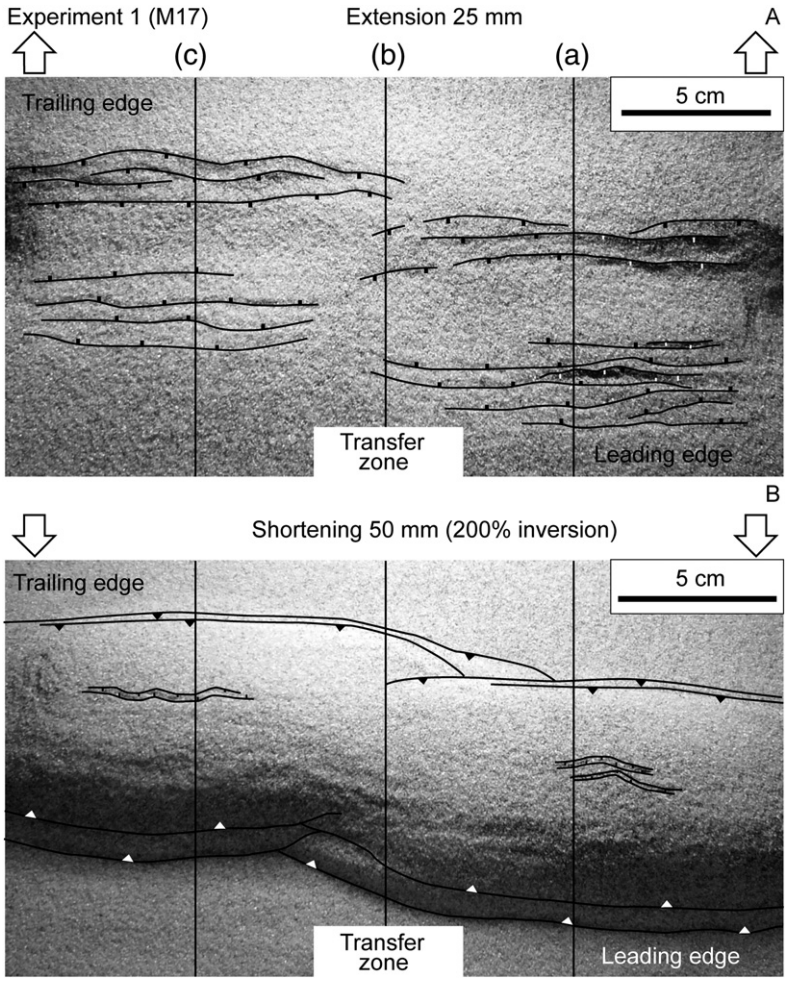

Fig. 7. Experiment 1. Photographs in plan view of model 17 at the end of extension (A) and at the end of shortening (B). Grabens were localised above the basal discontinuity induced by the limit of the mobile aluminium plate that was step-like in plan. Longitudinal propagation and overlapping rift culminations occurred above basement transfer structures during extension. Normal faults at the graben margins were reverse reactivated during inversion. The frontal ramps propagated laterally past the transfer structure. Late superficial normal faults were formed at the crest of the inverted graben after 200% inversion.

moving edge of the basal plate. Rift basins bounded by steep (58–65°) normal faults NF1 developed in sand layers (Figs. 5a–c and 6). These normal faults were formed by along-strike propagation and linkage of originally shorter, arcuate segments (Fig. 7A). The rift basins were characterised by a symmetrical geometry in cross-section (Fig. 5a–c). In plan view, longitudinal propagation and overlapping rift culminations occurred in the transfer zone (Fig. 7A).

During shortening, overturned folds formed in the strong ductile layer above the velocity discontinuity (Figs. 4a, 5a′–c′ and 6). The steep (58–65°) normal

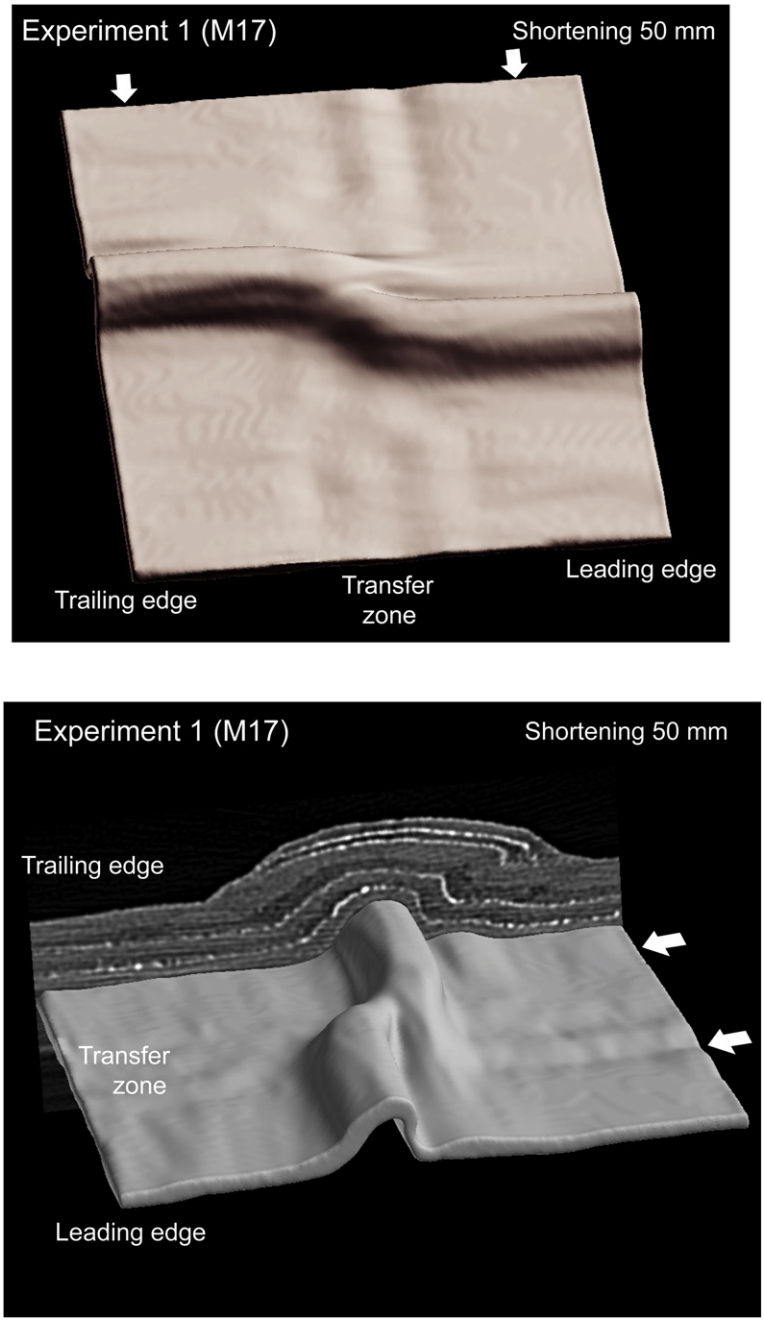

Fig. 8. 3D reconstructions of the frontal fold axes in ductile layers above the basement transfer structure between frontal ramps obtained from closely spaced CT image cross-sections for model 17. Deviation of the frontal fold axes was observed in ductile layers above the orthogonal offset zone orientation nearly parallel to shortening direction (white arrow).

faults at the rift margins in sand layers were reactivated as reverse faults; they were steep (50–65°) at depth and flattened (23–25°) near to surface (RNF; Fig. 6b–c). The reactivated faults progressively rotated to flatter dips (20–46°) after 100% inversion (Fig. 6d–e). New flatter (25°) thrust faults were subsequently formed outside of the original rift boundaries at the late stages of shortening (TF1–TF2; Fig. 6c–e). The sand layers filling the rift were deformed with the formation of fold-like structures in the inverted graben and on its margins (Figs. 4a and 5a′–c′). The deeper levels of the rift bounded by rift-margin faults were laterally compressed at a greater extent than the upper levels at the end of shortening (Fig. 6a, e). Late superficial normal faults NF2 were formed at the top of the inversion structure during the latest stages of shortening (Figs. 5, 6e and 7B). The leading frontal ramp propagated laterally into the footwall of the trailing ramp, and the trailing ramp propagated into the thrust sheet (Fig. 7B). In plan view, deviation of the frontal fold axis was observed within ductile layers above the orthogonal offset zone (Fig. 8).

3.2. Experiment 2 (M18)

In this model, sand layers and the strong ductile multilayer varied in thickness across the model to simulate a basal discontinuity created by previous stages of extension (Figs. 3b and 4b). The thicker edge of strong ductile multilayer was constructed above the mobile basal plate and it had the same orthogonal offset in plan view as the plate. The thicker edge of the multilayer was cut with a 47° dip towards the thinner edge to produce frontal and lateral ramps (Fig. 3b).

During extension, a master normal fault MNF developed in sand layers above the pre-existing frontal ramp in the strong ductile multilayer (Figs. 9a–c and 10). The

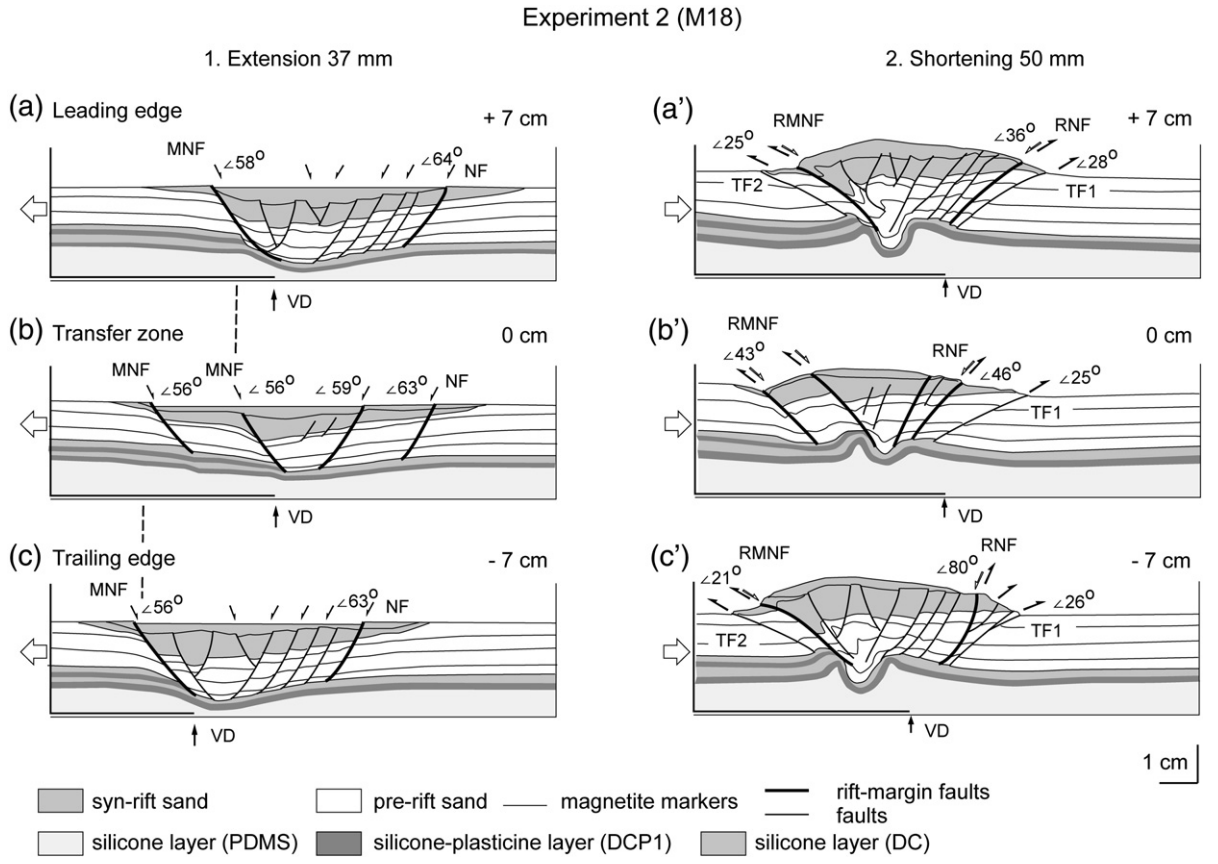

Fig. 9. Experiment 2. Drawings after X-ray CT image cross-sections for model 18 at the end of extension (a–c) and at the end of shortening (a′–c′). The location of the cross-sections in the model is shown in Figs. 3b and 12 (profile a). Variations in layer thicknesses controlled the rift localisation and its geometry, resulting in formation of asymmetrical rift and inversion structures. The master normal faults (MNF) developed above the thicker edge of the strong ductile multilayer in the model during extension (a–c), and they were reactivated as reverse faults (RMNF) during inversion (a′–c′). The thickness of synrift sand layers is less along the central cross-section in comparison to the edges of the model. NF = normal faults; RNF = reverse reactivated normal faults; TF = thrust faults; VD = velocity discontinuity.

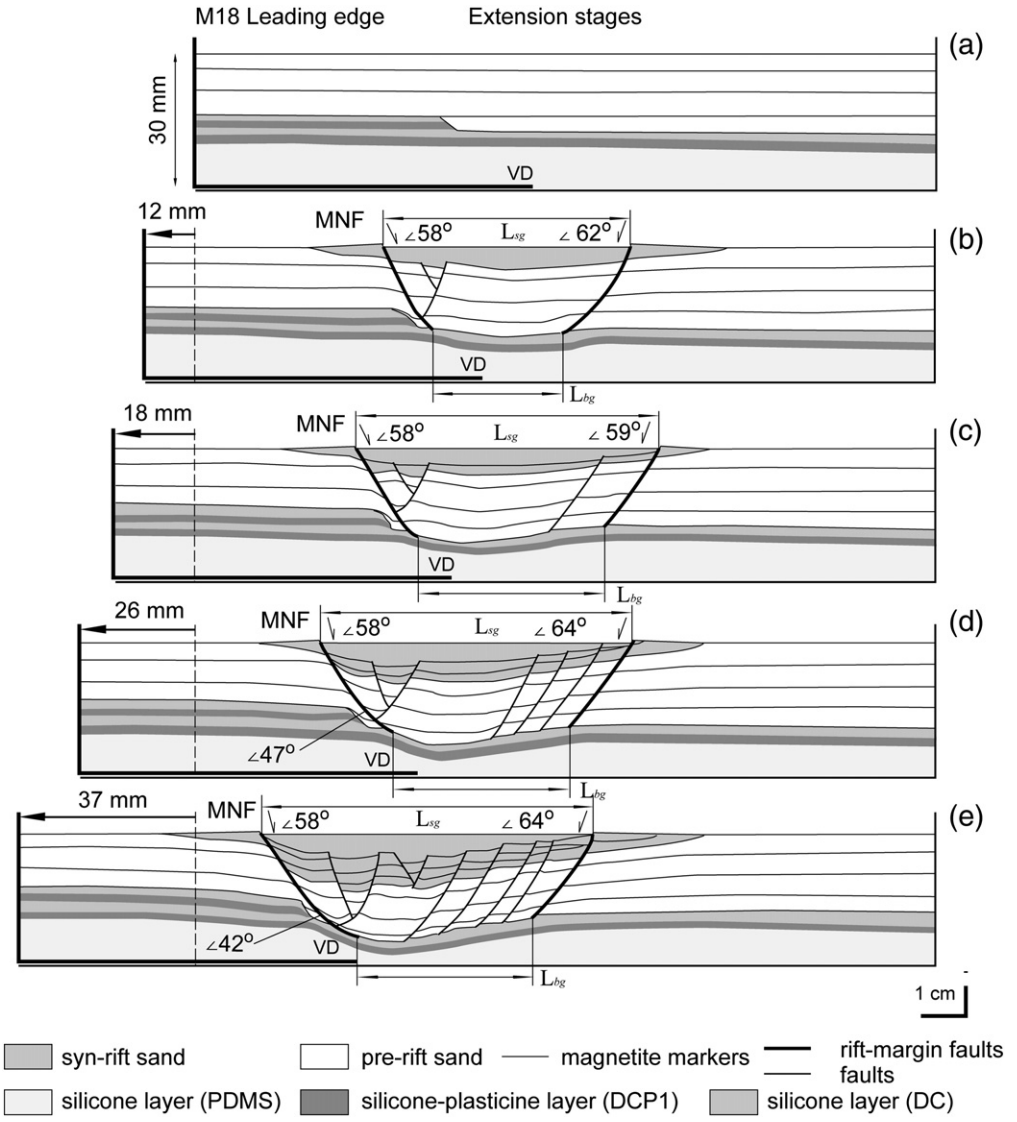

Fig. 10. Experiment 2. Drawings after X-ray CT images of scan sections across the leading part of model 18 obtained for subsequent stages of extension. Location of the cross-section is shown in Figs. 3b and 12 (profile a). The geometry of rift basin was asymmetrical. A steep (58°) master normal fault (MNF) developed above the thicker edge of the strong ductile multilayer in the model whereas a series of steeper (60–64°) normal faults progressively developed at the opposite side of the rift basin. See Fig. 9 for other symbols.

fault dipped in the same direction as the ramp and flattened with depth (58° at the upper and 42–47° at the deeper sand levels). This rift-margin normal fault was called "master" because it preserved its location through both extensional and shortening phases (Figs. 10, 11 and 12A). A series of arcuate, steep (60–64°) normal faults was progressively developed at the opposite side of the rift basin with continued extension (Figs. 9a, c, 10 and 12A). The geometry of rift basins was asymmetrical in cross-section, and the depth of the rift increased from the transverse zone to model margins (Fig. 9a, c). Longitudinal propagation and overlapping of the rift-bounding normal faults occurred in a transfer zone that developed above the orthogonal offset in the mobile basal plate and the lateral ramp in the strong ductile multilayer (Fig. 12A). Two *en relais* master normal faults were observed across the transfer zone (Figs. 9b and 12A) resulting from the simultaneous propagation of the rift-margin faults.

During shortening, reverse reactivation of the rift-boundary normal faults and bivergent thrusting occurred mostly along the rift margins (Figs. 9a′–c′ and 12B). Inversion structures were asymmetrical in cross-section, inheriting the geometry of extensional structures. The

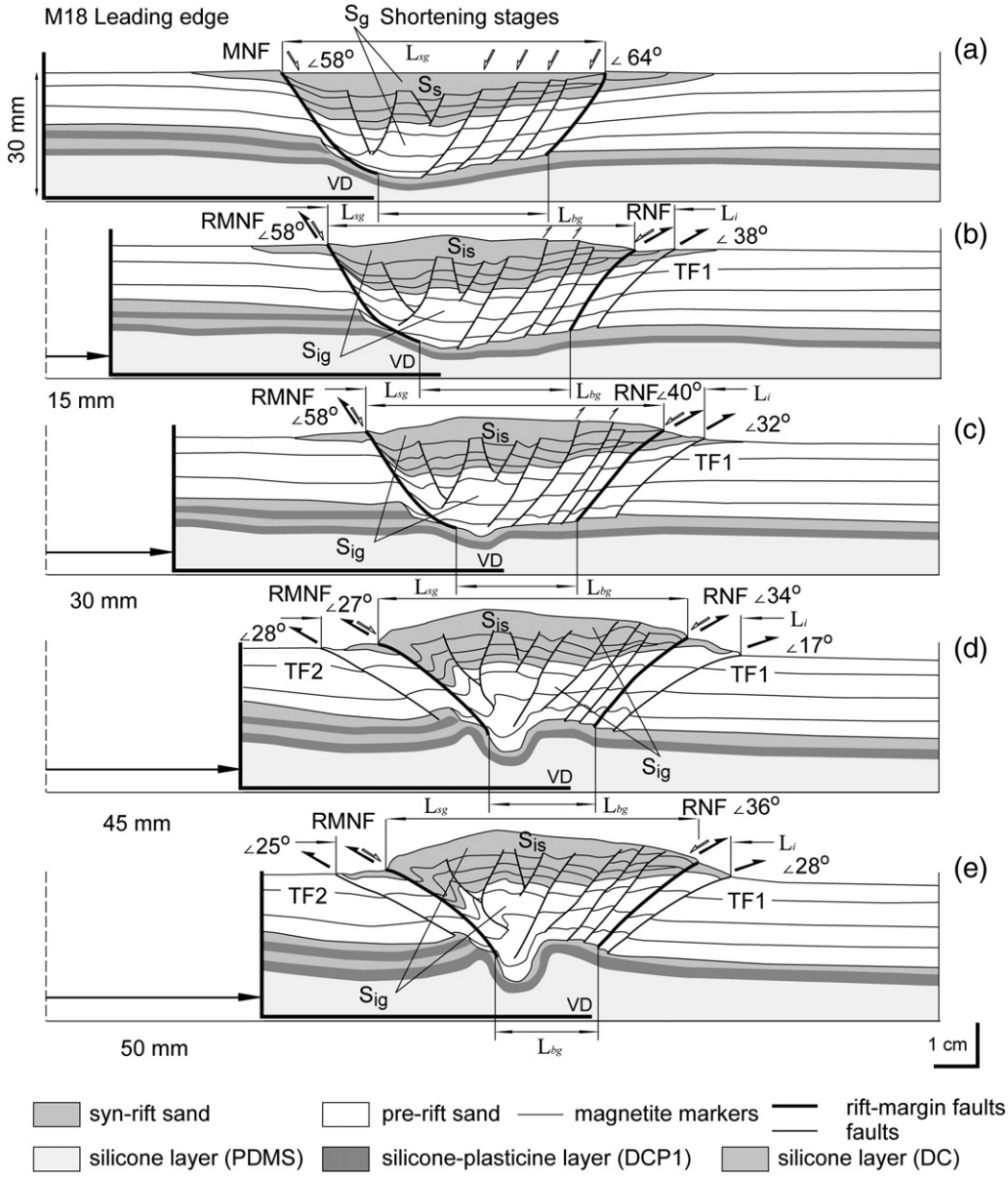

Fig. 11. Experiment 2. Drawings after X-ray CT images of scan sections across the leading part of model 18 obtained for subsequent stages of shortening. The location of the cross-section is shown in Figs. 3b and 12 (profile a). Inversion structures were asymmetrical in cross-sections, inheriting the geometry of the rift basin at the end of extension (a). The deeper levels of inversion structures were laterally compressed to a greater extent than upper ones and the central part of the rift was uplifted. Note the progressive changes of L_i (width of the inversion structure between external thrusts), L_{sg} and L_{bg} (graben width at surface and at base, respectively) measured between rift-margin faults (thick solid lines) and the progressive rotation and flattening of reverse reactivated normal faults after 100% inversion. See Fig. 9 for other symbols.

reverse reactivated master normal fault RMNF preserved the initial dip angle of 58° during the first stages of shortening, while reverse reactivated normal faults RNF at the opposite side of the inverted graben progressively rotated to become flatter (Fig. 11a–c). After 100% inversion, reverse reactivated normal faults at rift boundaries progressively flattened, and new thrust faults TF1–TF2 formed at the footwalls of the inversion structure (Fig. 11d–e). Progressive lateral compression of the inverted rift structures increased with depth for each stage of shortening. The deeper levels of the inverted graben bounded by reactivated rift-bounding faults (L_{bg}) were more compressed than the upper levels (L_{sg}). The layers filling the rift structure were uplifted

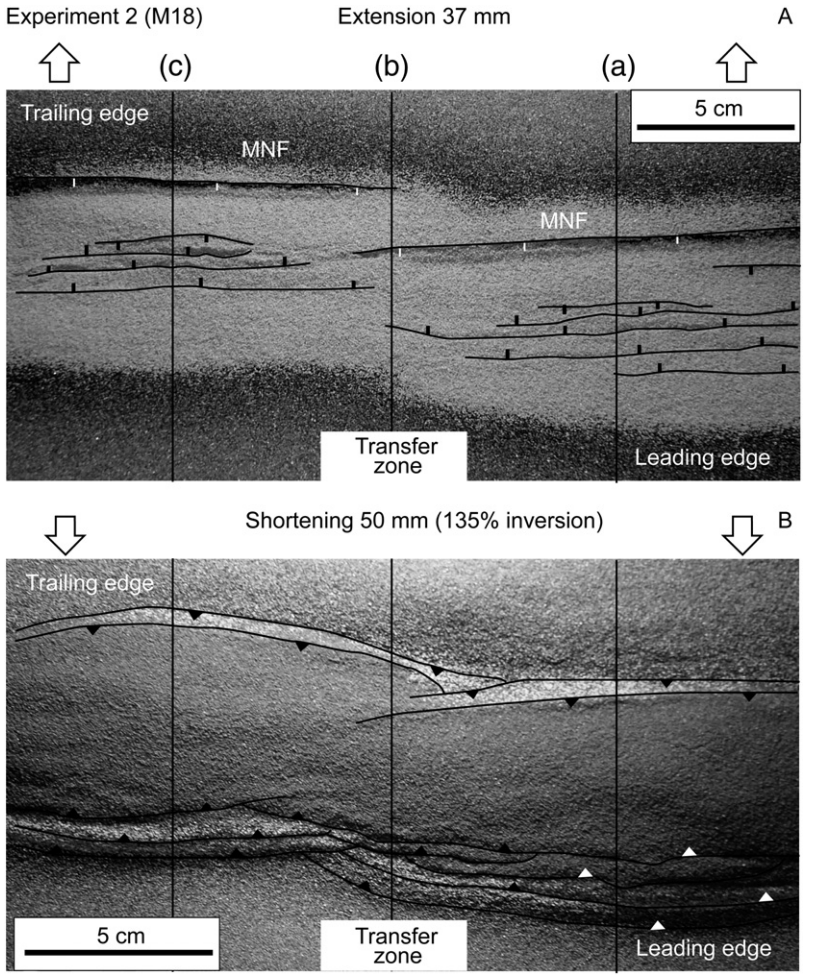

Fig. 12. Experiment 2. Photographs in plan view of model 18 at the end of extension (A) and at the end of shortening (B). Grabens localised above the basal discontinuity are asymmetric. The long master normal faults (MNF) developed on rift margins above frontal ramps in the ductile layer. MNF preserved their location throughout extension, while a series of shorter arcuate normal faults developed on the opposite rift margin. Longitudinal propagation and overlapping rift culminations occurred in a transfer zone during extension (A). Reverse reactivated normal faults and new flatter thrusts propagated laterally past the transfer structure during inversion (B).

(Figs. 9a′–c′, 11 and 12B)). Marker sand layers in the inverted graben showed fold-like structures in the rift and on the rift margins (Figs. 4b and 11).

3.3. Experiment 3 (M20)

In the third model, the strong ductile multilayer had a constant thickness but varied in rheology across the model (Figs. 3c and 4c). A multilayer of silicone putty (DC) mixed with 44% modelling putty was used to create a “stronger” margin and the same DC without modelling putty was used for the “weaker” margin of the model. The contact between the two materials was cut with a dip of 54° toward the weaker margin. The contact between them was filled with low viscosity PDMS, which was also used for the weak basal ductile layer. In plan view, the prescribed cut between ductile basal layers of differing rheology had an orthogonal offset. In contrast, the geometry of the mobile thin aluminium plate at the base of the model remained constant along its strike. The limit of the aluminium plate was located under the boundary between stronger and weaker margins for the leading edge of the model and it was found under the stronger margin for the trailing edge of the model (Fig. 3c).

At the beginning of extension, the steep planar master normal faults MNF were localised in sand layers above the prescribed cut between ductile layers of differing composition, dipping at 62–69° toward the weaker margin of the model (Figs. 13 and 14a–c). The

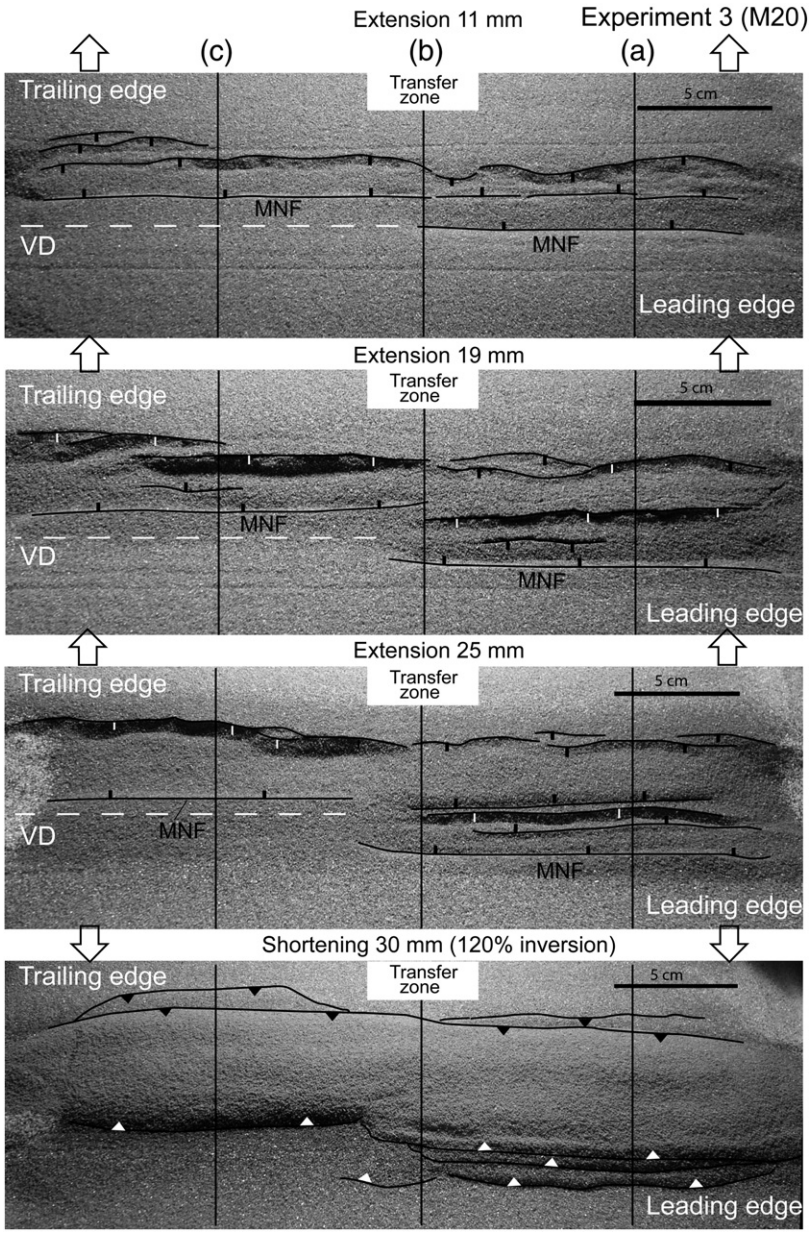

Fig. 13. Experiment 3. Photographs in plan view of model 20. During extension (3 upper photos), the rift basins were localised above the boundary between the model margins with different compositions. The geometry of the basal aluminium plate (VD = velocity discontinuity) did not affect rift localisation. At the end of shortening (lower photo), the inverted grabens were uplifted, and new thrust faults propagated laterally past the transfer basal structure. MNF = master normal fault.

geometry of the basal mobile plate (VD) did not affect rift basin localisation remaining under the "stronger" margin (Fig. 13). The main rift-margin fault preserved its location and geometry during continued extension (Figs. 13, 14 and 15a–c). A series of arcuate and short, steep (64–67°) normal faults was developed at the ramp margin of the rift basins and the faults were progressively linked with continued extension (Fig. 13). The ramp margin faults were located above the moving edge of the strong ductile multilayer in the trailing part of model (Fig. 14c). These faults developed above the surface curvature and thinning in ductile layers in the leading part of the model (Figs. 14a and 15a–c). Two rift basins formed in the leading part of the model due to progressive thinning and extension of ductile layers (Fig. 15a–c). Longitudinal propagation and overlapping

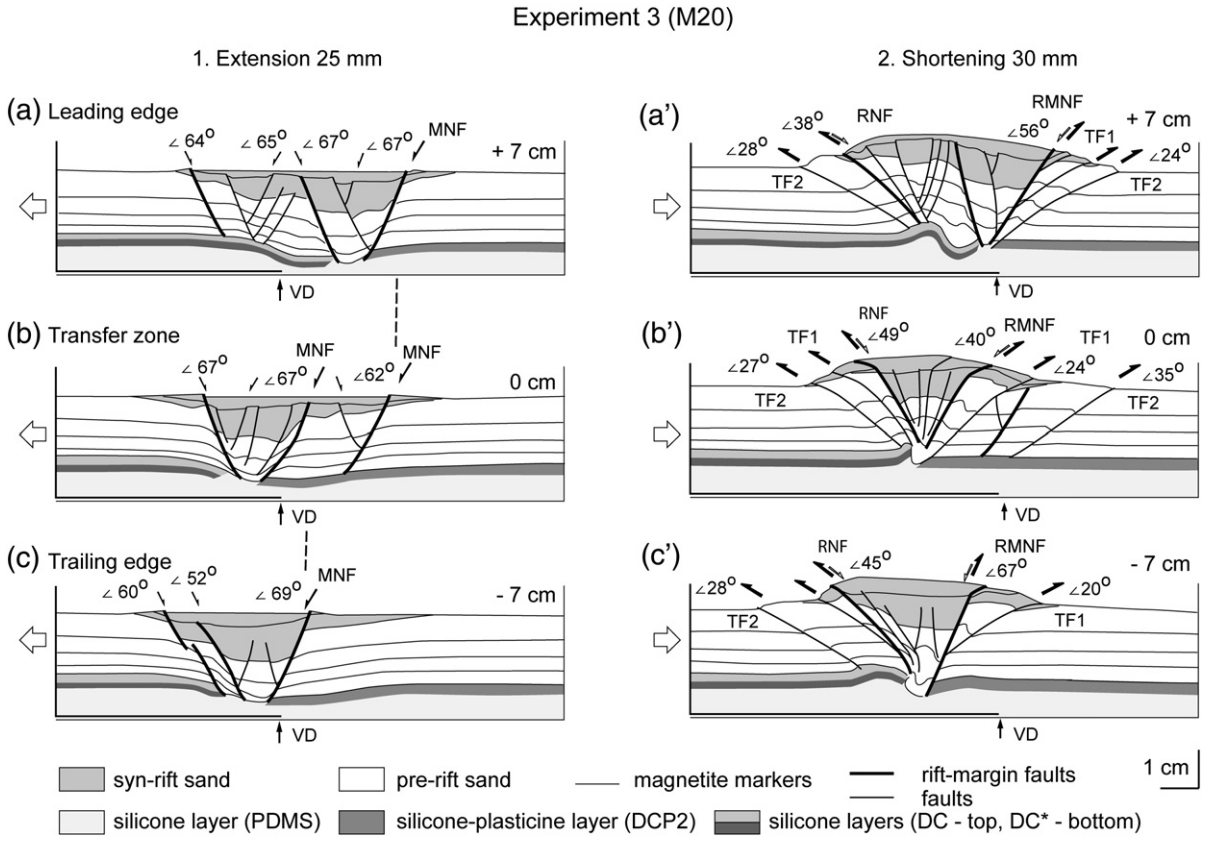

Fig. 14. Experiment 3. Drawings after X-ray CT images of scan cross-sections of model 20 at the end of extension (a–c) and at the end of shortening (a′–c′). The location of the cross-sections of the model is shown in Figs. 3c and 13 (profile a). Master normal faults (MNF) were localised in the brittle sand layer above the boundary between different strong ductile layers, dipping from the stronger towards the weaker model margin. During shortening, bivergent thrusts developed at the rift margins due to reactivation of normal faults and new thrust faults were formed. See Fig. 9 for other symbols.

of rift basins resulted in the formation of two *en relais* master normal faults MNF in the transfer zone (Figs. 13 and 14b).

During shortening, asymmetrical inversion structures were formed (Figs. 14a′–c′ and 15d–e) through bivergent thrusting at the rift margins due to reactivation of normal faults and formation of new thrust faults. During the first stages of shortening, steep normal faults at rift margins were reactivated as reverse faults at the same dip angle 64–66° (Fig. 15d). The newly formed flatter thrust faults TF1 developed in the footwall of the reactivated master normal fault (RMNF) to accommodate increasing shortening (Fig. 15d). Following further shortening (but <100% inversion), the RMNF preserved the same steep dip angle, while the reactivated normal faults and new thrust faults rotated to become flatter, with dips of 42° and 30°, respectively (Fig. 15e). At late stage of shortening (>100% inversion), all faults rotated to become flatter and new thrust faults TF2 formed outside the initial graben (Fig. 15f). The interior of the inverted rift basin had progressively undergone lateral compression, which was greater for deep levels of the model (Fig. 15d–e). The rift filling layers were uplifted with rotation and tilting on the rift margins (Figs. 4c, 14a′–c′ and 15d–e).

3.4. Analysis of particle trajectories across the inversion structure during shortening

Marker particle trajectories were traced to quantitatively analyse deformation patterns and distribution of shortening across the inversion structure in the leading edge of model 18 (Experiment 2). The variations in graben width at the surface (L_{sg}) and at its base (L_{bg}) and in width of the inversion structure (L_i) were estimated for successive stages of shortening (Fig. 11). The marker particles were traced on CT scan profiles through successive stages of shortening of the same cross-section (Fig. 11) to obtain particle displacement paths (Fig. 16a). The distance between the marker particles was calculated to estimate internal deformation across the graben (Fig. 16b).

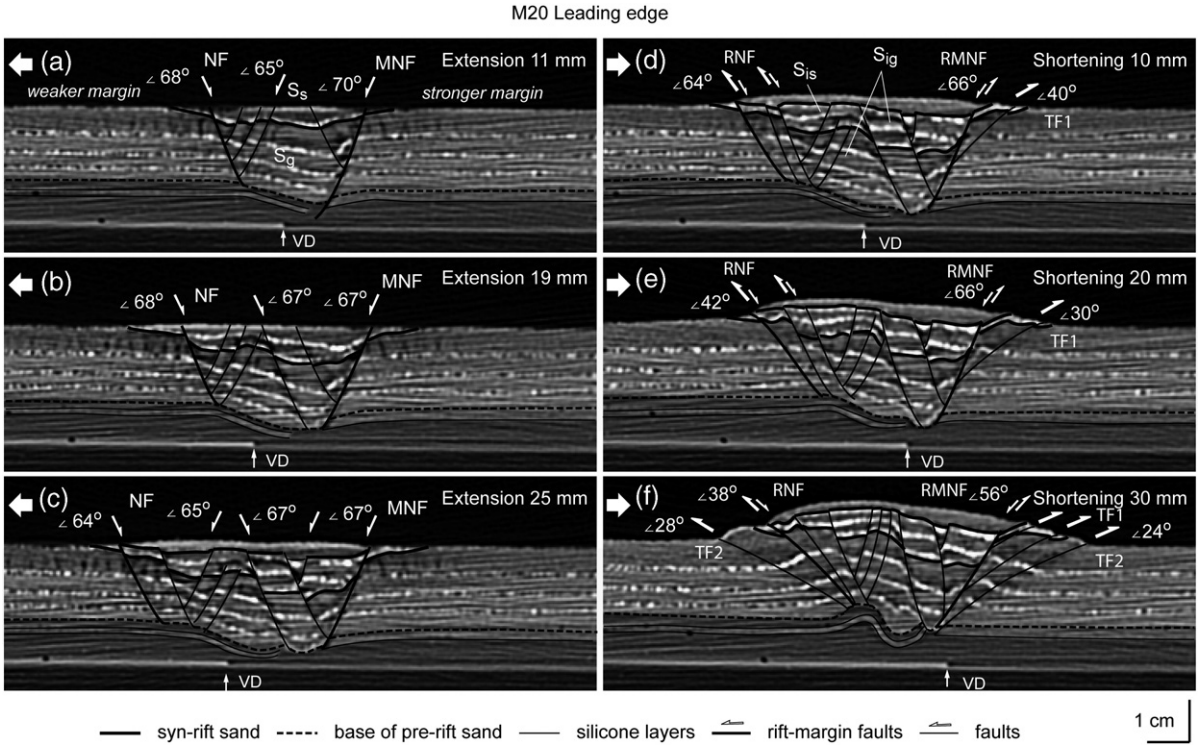

Fig. 15. Experiment 3. X-ray CT images of scan sections across the leading part of model 20 obtained for subsequent stages of extension (a–c) and shortening (d–f). Location of the cross-section is shown in Figs. 3c and 13 (profile a). During extension, master normal faults (MNF) preserved the same location, while a series of normal faults (NF) developed on the opposite margin of the rift. During shortening, steep normal faults were initially reverse reactivated (d–e), then rotated and flattened after 100% inversion (f). Layers filling the rift basins progressively underwent lateral compression, which was greatest for deep levels of the model. See Fig. 9 for other symbols.

At the end of shortening, the width of the inversion structure (L_i) increased by 23% compared to its width at the beginning of shortening (Fig. 17a) through formation of new thrust faults TF1 and TF2 at the model margins (Fig. 11). The variation in width of the inversion structure was cyclic. Once a new thrust fault TF1 formed, the structure widened by 8% (Fig. 17a, peak 1), then it became relatively narrow (3%) due to lateral compression and reactivation of faults at its interior (Fig. 17a, peak 2). The cycle was repeated with 25% widening of the structure after formation of the thrust fault TF2 (Fig. 17a, peak 3) and the following stage of 7% relative shortening (Fig. 17a, peak 4).

During shortening, the graben width at the surface (L_{sg}) was more stable than the width of the inversion structure (L_i) (Figs. 11 and 17a). The graben became 9% narrower during the first 30 mm of shortening due to lateral compression (Fig. 17a). Then, it became 6% wider during the next 20 mm of shortening reflecting relative extension at the surface. In contrast, the graben width at its base (L_{bg}) narrowed progressively to become 38% narrower after shortening was completed (Figs. 11 and 17a). The variations in graben width at the surface and at its base likely reflect the unequal distribution of internal deformation across the inversion structure during shortening. The deeper levels of the structure were more compressed, and the material was pushed up and outwards creating a zone of local extension near the surface (Fig. 11). The best evidence for late near-surface extension in the inversion structure is the presence of local normal faulting at the top of model 17 (Experiment 1) at the end of shortening (Figs. 4a and 7B).

To quantify the deformation distribution across the inversion structure, the horizontal and vertical displacements of marker particles and the distances between them at the deep and upper levels of the inversion structure were calculated for each stage of shortening for the leading edge of model 18 (Fig. 16b). The horizontal distances between marker particles 2–3 and 3–5 at the base of the model progressively diminished (Fig. 17b), confirming contraction has occurred at the deep levels of the model. The distances between the marker particles at the upper level of the model (1–4, 4–7, 7–8, 8–6) changed from stage to stage, diminishing during the first 15 or 30 mm of shortening and increasing during the later stages of shortening (Fig. 17b). The increase of

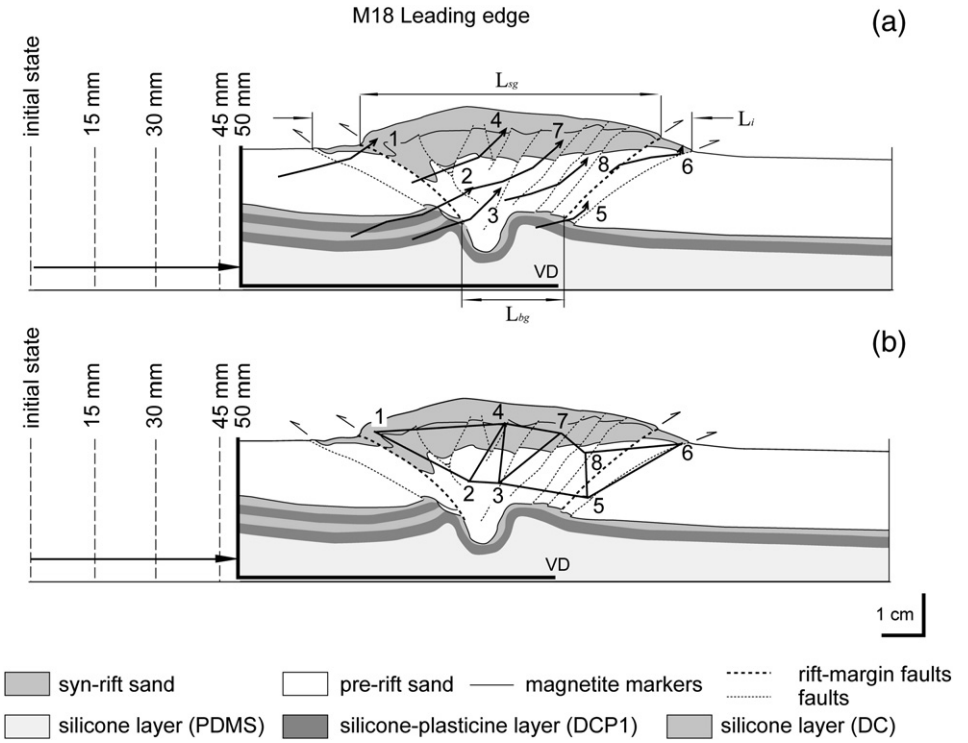

Fig. 16. Displacement paths of marker particles (a) and the distances between them (b) traced for the leading part of model 18 derived from X-ray CT images for successive stages of shortening (see Fig. 11). Location of the cross-section is shown in Figs. 3b and 12 (profile a). The dashed line shows the rift-margin faults. The width of graben at the surface (L_{sg}) and at its base (L_{bg}) was determined as the distances between the most external normal faults delimiting graben at the surface and at the base, respectively (Figs. 10 and 11). L_i is determined as the distance at the surface between the most external active thrust faults at the margins of inversion structures (Fig. 11).

distances between the shallow marker particles confirms that local extension occurred near the surface of the inversion structure during the late stages of shortening. The described changes of horizontal distances between upper markers (Fig. 17b) are in good agreement with the variations of graben width at the surface L_{sg} (Fig. 17a) that decreased during the first 30 mm of shortening and then increased during the last 20 mm of shortening.

The vertical distances between marker particles generally increased with shortening, especially for the outside pairs of particles 1–2, 5–6, 5–8 (Fig. 17c). Only the distance between the middle particles 2–4 diminished progressively with shortening because of the higher rate of vertical displacement of particle 2 relative to the same value of particle 4. Vertical displacements are highest for the marker particles 2 and 3 located at depth within the graben (Fig. 18a), confirming progressive vertical extrusion of basal material across the inversion structure. The particle 5 located at depth outside the graben underwent less uplift. The shallow particles (1, 4, 7 and 8) were displaced upward at a slower rate relative to the deep-seated particles (Fig. 18a).

The horizontal displacements of marker particles located inside the graben diminished, while their vertical displacements increased after 30 mm of shortening (Fig. 18a, b). This effect was observed in the particle paths which became steeper after 30 mm of shortening (Fig. 17a). Particle 6 located near the surface, but outside the graben was displaced mostly horizontally (Fig. 16). This particle is found above the frontal thrust fault TF1, and its movement likely reflects progressive material displacement in the hanging wall of the fault during continuing shortening (Fig. 11). The frontal thrust TF1 rotated with changes of dip angle from 50° to 32°. The predominance of vertical movement of marker particles relative to their horizontal displacement inside the inverted graben (Fig. 18c) is likely the effect of increasing lateral shortening at deep levels of the structure and upward extrusion of material.

3.5. Analysis of lateral compression across the inversion structure during shortening

Analysis of CT scans of model cross-sections from successive inversion stages leads to the observation that

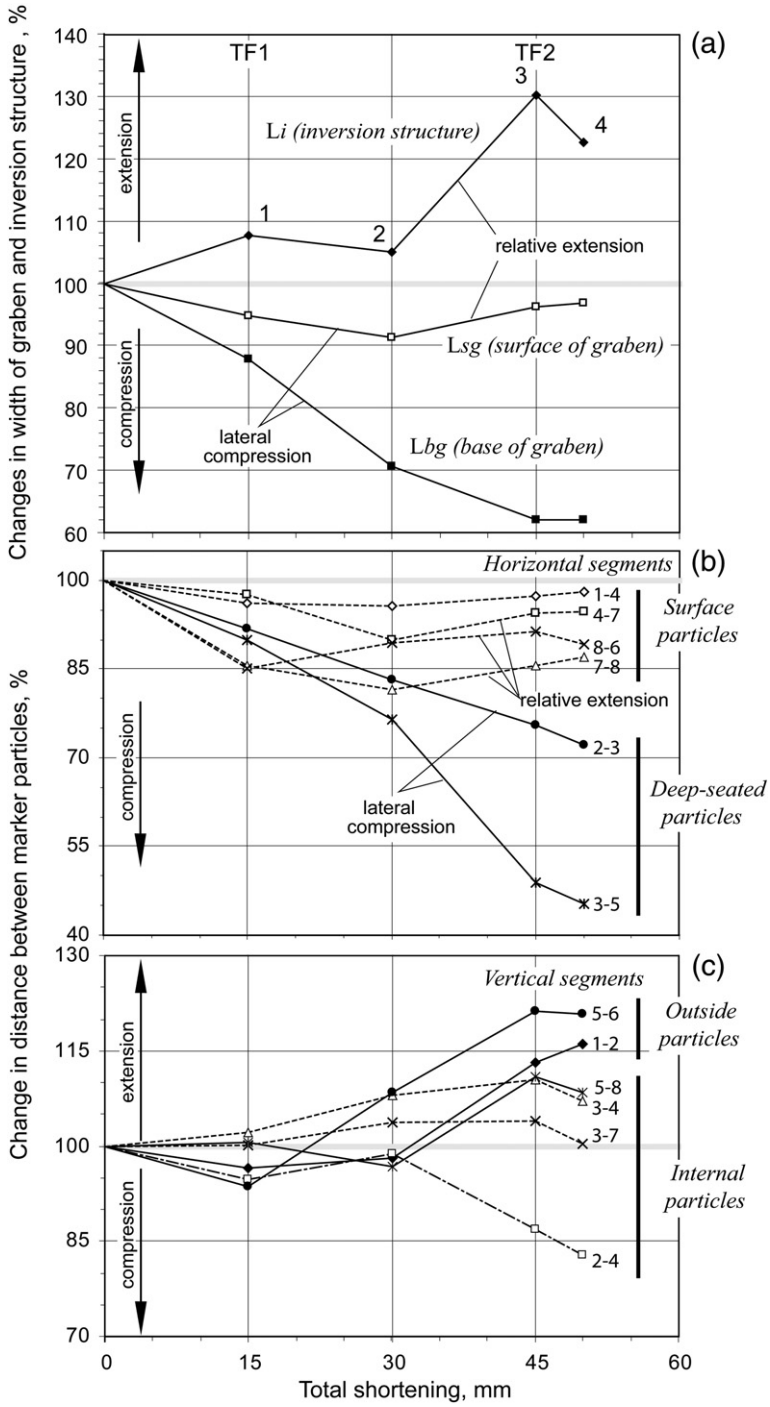

Fig. 17. Diagrams showing variations of (a) widths: width of the inversion structure (L_i), graben width at the surface (L_{sg}), and graben width at its base (L_{bg}); and of (b) horizontal and (c) vertical distances between marker particles during shortening obtained for the leading part of model 18 (Fig. 16). The width of the inversion structure (L_i) grew by 23% due to the formation of new thrust faults TF1 and TF2 (Fig. 11). The graben width at its base diminished greater than at its surface during shortening, reflecting greater lateral compression at deep levels (Fig. 11). The horizontal distances between deep-seated marker particles also diminished in comparison to subsurface particles. The vertical distances between marker particles generally increased with shortening.

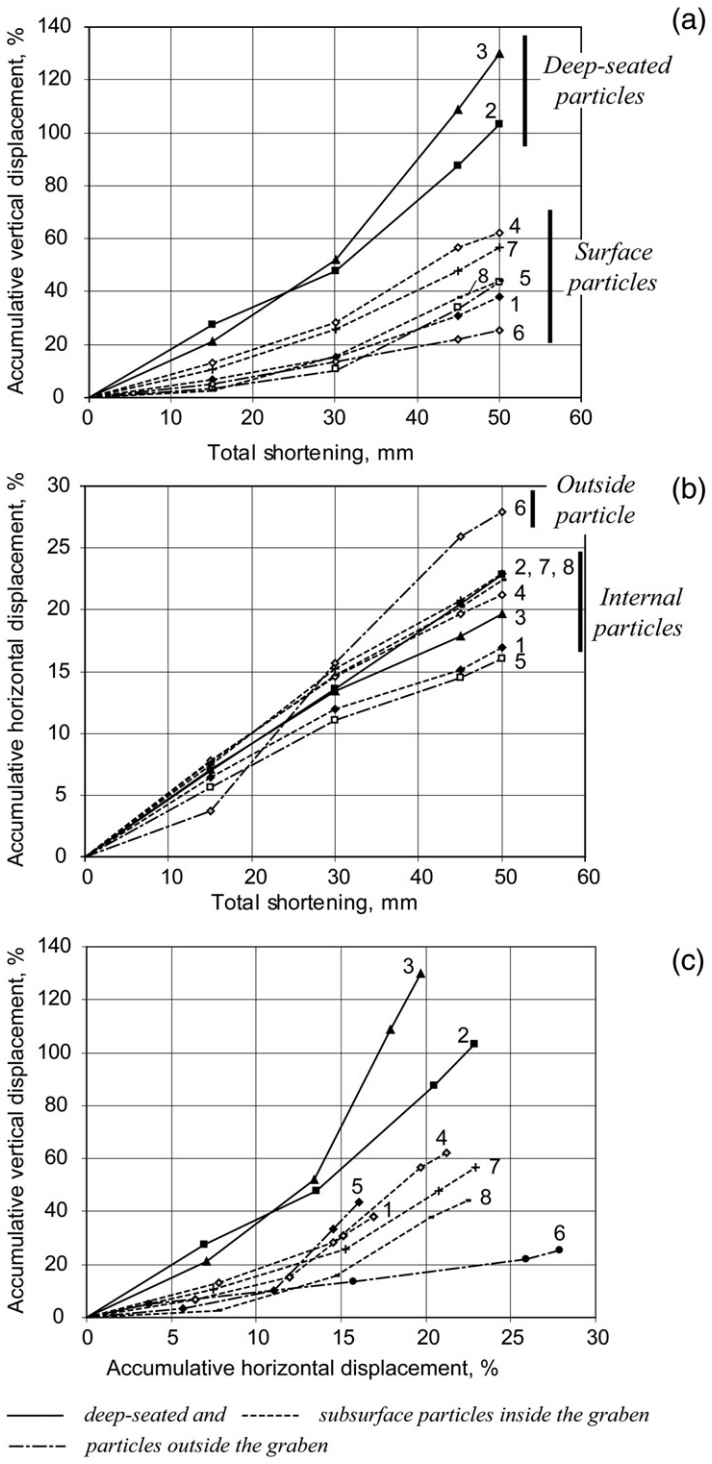

Fig. 18. Diagrams showing the accumulative percentage of horizontal and vertical displacements of marker particles (Fig. 16). The vertical displacement of marker particles dominates over their horizontal displacement inside the inverted graben reflecting the effect of increased lateral compression at deep levels and upward extrusion of material.

the deeper levels of inverted graben bounded by reactivated normal faults were laterally compressed to a greater extent than at shallower levels (Figs. 6a–e, 11a–e and 15d–e). The quantitative analysis of marker particle displacement for one of the models (Fig. 17b) presented above confirms this observation. To analyse lateral compression, the areas of inverted graben and of synrift sand layers were calculated in model cross-sections for each stage of shortening (Figs. 6, 11 and 15). The calculated area of inverted graben S_{ig} is limited by the reactivated rift-margin normal faults RNF and RMNF shown by thick solid lines, and the area of inverted synrift fills S_{is} is shown in grey (Figs. 6, 11 and 15).

The areas of inverted graben S_{ig} progressively diminished (up to 24%) following shortening in comparison to their areas at the late stage of extension S_g (Fig. 19a). Such shortening reflects the increase of lateral compression in inverted graben that is likely accommodated by volume loss through porosity reduction in model sand layers. The areas of synrift sand-filled basins S_{is} diminished during the first 15 mm of shortening (Fig. 19b) and then slightly increased (M18), or stayed nearly the same (M20) as at the late stage of extension S_s, or S_{is} progressively increases (M17) with shortening. The relative areal increase of synrift basins during inversion and graben uplift seems to be the consequence of lateral extension with increase of volume and porosity of the upper levels of the models. This conclusion is in good agreement with the changes of horizontal distances between marker particles in the upper levels of model 18 (Fig. 17b) and with the variations of the graben width at the surface L_{sg} (Fig. 17a), which diminish during the first stages of shortening and increase during its later stages. The greatest increase in lateral extension (up to 21%) in the synrift sand-filled basin is observed for model 17 during late stages of shortening (Fig. 19b). This may be explained by the fact that model 17 underwent the greatest (200%) extent of inversion relative to the other experiments here (Fig. 4). The synrift basins of this model are the shallowest, and they are more uplifted than in other experiments (Figs. 5, 9 and 14). To support our analysis, local extension at the surface of inversion structures was observed in this model during the late stages of shortening (Fig. 7B).

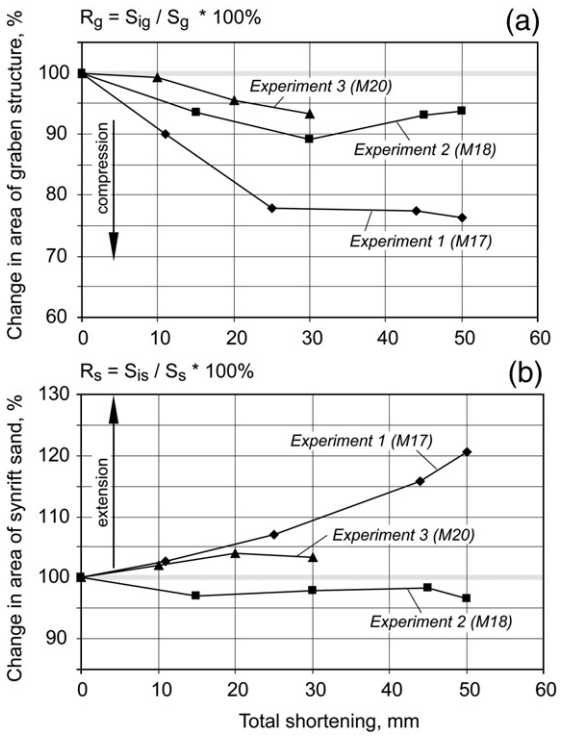

Fig. 19. Diagrams showing percentage changes in area of graben R_g (a) and synrift sand-filled basins R_s (b) during inversion calculated for model cross-sections across their leading edges (Figs. 6, 11 and 15). The calculated area of graben is limited by bounding reverse reactivated normal faults RMNF and RNF. $R_g = S_{ig}/S_g$, $R_s = S_{is}/S_s$, where S_g and S_s = areas of graben and synrift sand at the last stage of extension, respectively, and S_{ig} and S_{is} = areas of inverted graben and synrift sand at each stage of shortening, respectively.

4. Discussion

4.1. Geometry of faults during extension

The location and geometry of normal faults at rift margins differ in the described models depending on variations in the geometry and rheology of ductile basal layers. Symmetrical rift basins were formed in the model with initially constant thickness and composition of ductile layers (Fig. 5). Rift-bounding faults were closely spaced, slightly arcuate, and of similar steep dip. The location and geometry of normal faults at rift margins in sand layers were controlled by symmetrical thinning of ductile layers above the velocity discontinuity. Asymmetrical rift basins formed in the models with initial variations in thickness or rheology of ductile layers (Figs. 9 and 14). A single long, nearly planar, steep master normal fault bounded one side of rift basins and a series of shorter, closely spaced arcuate steep normal faults developed along the opposite side of rift basins. The location and dip of master normal faults at rift margins in sand layers were controlled by variations in thickness and ramp inclination in basal strong ductile multilayer (Fig. 9) or by changes in rheology and the prescribed cut in the same multilayer (Fig. 15).

Rift-bounding normal faults formed by along-strike propagation and linkage of originally shorter, similarly

dipping segments in our models (Figs. 7A, 12A and 13) are similar to those observed in natural examples (Larsen, 1988; Peacock and Sanderson, 1994; Childs et al., 1995; Peacock, 2002). Patterns of initial fault segmentation and subsequent linkage, similar to our models, were obtained in numerical models (Cowie et al., 2000), and also have been imaged in three-dimensional seismic studies of Jurassic faults in the Viking Graben, North Sea (McLeod et al., 2000).

4.2. Inversion and fault reactivation

At the beginning of shortening, the *steep* rift-margin normal faults in our models were reactivated in sand layers as reverse faults with steep dip angles (58–67°). CT scans provided clear images of this process (Figs. 6, 11 and 15). Reactivation of steep normal faults in the models was obtained during bulk *horizontal* shortening and not by *vertical* block movement as in the experiments of Koopman et al. (1987). Folding of ductile layers under horizontal shortening resulted in the transfer of pure *horizontal* displacement of the moving wall to *vertical* displacement of the surface of ductile layers that, in turn, transferred deformation to overlying sand layers. This setting was likely favourable to reactivate *steep* fault planes in sand layers.

After 100% inversion, reactivated normal faults rotated to become progressively flatter (19–38°) with continued shortening similar to the experiments of Mitra (1993). The new flatter thrust faults formed outside of the inverted graben with (20–34°) dip angles (Figs. 6c, 11c and 15f)) similar to the analogue experiments of Panien et al. (2005) and Eisenstadt and Withjack (1995). In experiments with asymmetric graben (M18, 20), the master normal fault preserved steep dip until the latest stages of shortening and rotated less than reactivated normal faults at the opposite side of the graben, resulting in an asymmetric geometry of inversion structure (Figs. 11 and 15d–f). During shortening, inverted graben structures in our models inherited the geometry from pre-existing rift basins forming symmetrical or asymmetrical structures in cross-section (Figs. 5, 9 and 14). The layers filling the rift structures were laterally compressed at depth, pushed up and uplifted (Figs. 5, 9 and 14a′–c′). Marker sand layers in the inverted graben illustrated fold-like structures (Figs. 4a, b, 6 and 11) or rotation and tilting (Figs. 4c and 15d–f) in the rift and on the rift margins.

Reverse reactivation of steep normal faults is known from the example of the eastern Sunda shelf, where Cenozoic grabens (Fig. 20) underwent inversion during the Middle Miocene (Letouzey et al., 1990). The authors noted that the dip of the main normal faults bordering the active grabens and half-grabens was generally about 60°–80°, while a lower dip (45°) of normal faults was inferred for deeper structural levels. Letouzey et al. (1990) suggested that, in weakly inverted grabens, reverse slip movement occurred only in the deeper level of the reactivated normal faults, while folding and flexure above the pre-existing fault plane accommodated shortening in the upper levels of the grabens. Nevertheless, with strong regional shortening, large uplifts and thrust faults were observed with reverse reactivation along pre-existing steeply dipping normal fault planes even at high structural levels in strongly inverted grabens (Fig. 20), similar to our experiments (Figs. 4, 6c, 11b–c and 15d–e). The reverse movement in strongly inverted grabens was accompanied by the propagation of the new reverse fault plane, which tended to flatten at shallow levels (Letouzey et al., 1990). The strongly inverted grabens on the eastern Sunda shelf were those whose orientation was perpendicular to the regional shortening that corresponds to the setting of the co-axial shortening in our experiments. Basement blocks and sediment fill in the grabens were tilted and rotated or demonstrated buckling, flexuring and folding of sedimentary cover during inversion (Letouzey et al., 1990) similar to our models (Figs. 4, 6, 11d–e and 15d–f).

Rift faults in the experiments of Gartrell et al. (2005) actually steepened during shortening and eventually locked up followed by cut-off thrust development. In our models, the rift faults rotated and flattened during shortening (Figs. 6, 11 and 15), and hence became more ideally oriented for reverse movement. This appears to be due to the nature of the deep level folding. In the models of Gartrell et al. (2005), folds developed were of longer wavelength and the uplifted areas occurred on the rift basin margins, whereas the rift axis formed a depression during inversion. This is different from the models presented here where the whole graben area experienced uplift (Figs. 6, 11 and 15). This may be due to the difference in thickness of the middle crustal layer that was thicker in the models of Gartrell et al. (2005). These contrasts illustrate the importance of the middle crustal layer in controlling upper-crustal deformation styles. The greater extent of inversion (120%–200%) and its orthogonal orientation in the experiments here could also contribute to the differences observed in our models in comparison with the models of Gartrell et al. (2005), in which less shortening (86% inversion) and oblique inversion were applied.

Eisenstadt and Withjack (1995) showed that the amount of inversion influenced the fault and fold geometries developed in the inverted half grabens of the clay models. Reverse reactivation of steep (60°–70° of dip)

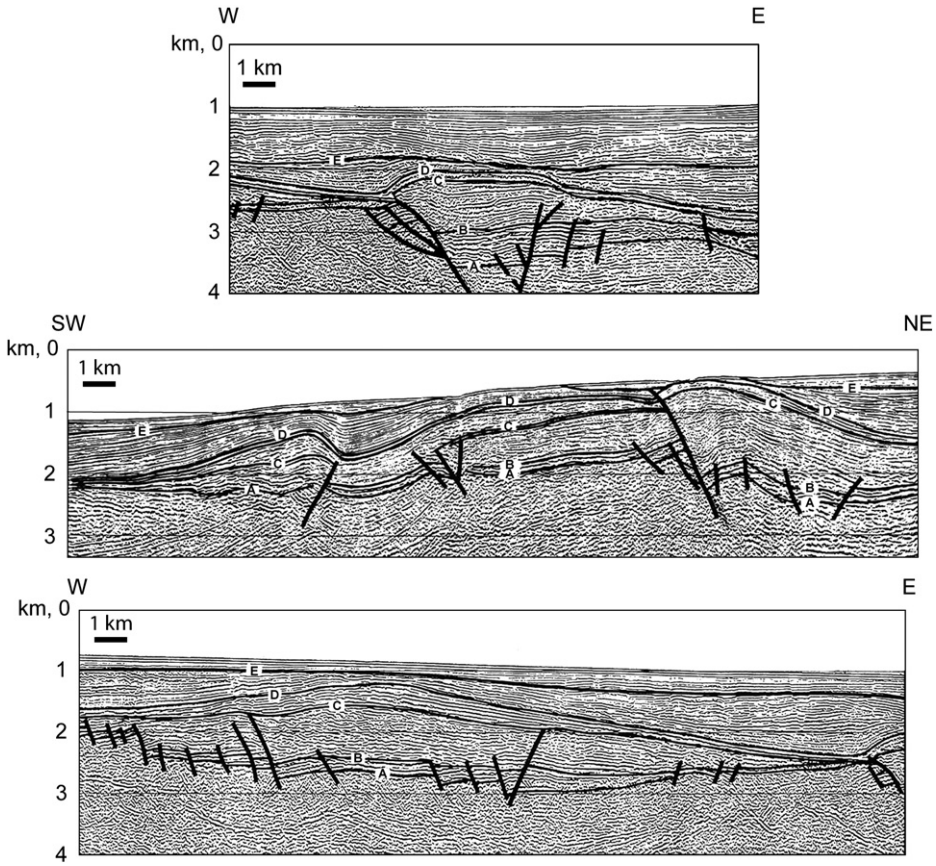

Fig. 20. Seismic sections (depth converted) showing graben inversion in the eastern Sunda shelf, after Letouzey et al. (1990; Copyright Elsevier, reprinted with permission).

normal faults was observed in the half graben only with 50% of inversion, while reactivation ceased between 50% and 100% inversion and low-angle thrust faults with small displacement accommodated the most shortening. With 200% inversion, low-angle thrust faults with large displacements cut the main normal fault and many of the secondary normal faults (Eisenstadt and Withjack, 1995). These results are partially similar to our models, in which normal faults on rift margins underwent reverse displacement preserving initial high dip angles during the first stages of shortening (Figs. 6b–c, 11b–c and 15d–e). However, with more than 100% inversion, the reverse reactivated normal faults in our models rotated and flattened to actively accommodate continuous shortening along with low-angle thrusts developing later (Figs. 6d–e, 11d–e and 15f). This is different from the models of Eisenstadt and Withjack (1995), in which secondary normal faults only passively rotated and uplifted during increasing inversion and most shortening was accommodated by active low-angle thrusts. The difference in behaviour of reactivated normal faults is likely related to the deep level folding that occurred in our models as discussed above and underlines the importance of the middle crustal layer in controlling upper-crustal deformation styles.

A broad anticline formed at shallow levels above the original half graben after 50% of inversion expanded laterally and vertically with progressive shortening and finally changed to a syncline in the lower growth layers and to an anticline in the pre-growth layers (Eisenstadt and Withjack, 1995). This is similar to the geometry of the structures imaged by the progressive displacement of the sand layer markers in the rift filling layers analogical to folding and flexuring (Figs. 4a, b, 6 and 11) or rotation and tilting (Figs. 4c and 15d–f) in the rift and on the rift margins.

4.3. Transfer zones

Transfer zones developed in our models during extension were characterised by overlapping rift-bounding normal faults and interlocking fault arrays (Figs. 7A,

12A and 13) similar to natural examples (Corfield and Sharp, 2000; Gawthorpe and Leeder, 2000; Morley and Wonganan, 2000; Peacock, 2002) and to previous numerical (Cowie et al., 2000) and analogue experiments (Acocella et al., 1999; McClay et al., 2002; Hus et al., 2005; Gartrell et al., 2005). Propagating tips of rift-margin faults in transfer zones resulted in the formation of two offset sub-basins oriented at right angles to the extension direction (Figs. 5, 9 and 14). The presence of a basal offset in our models did not produce a discrete extension-parallel transfer fault in sand layers, contrary to the sand models of Hus et al. (2005) and Gartrell et al. (2005), in which a new connecting fault was observed. It is considered that a hard-linked transfer fault was not formed in our models because no through-going basement fault was included in the present experiments. These experiments represent a different scenario where there is a sharp offset in basement geometry. Extensional fault patterns without discrete, hard-linked strike-slip transfer faults, similar to our models, have been observed in the East African–Ethiopian rift system (Morley et al., 1990; Hayward and Ebinger, 1996) and in analogue models of O'Brien et al. (1996, 1999).

During shortening, frontal thrust faults propagated simultaneously and deflected as oblique ramps in transfer zones (Figs. 7B, 12B and 13) similar to the experimental results of thrust wedges with horizontal offsets of a backstop (Calassou et al., 1993). At deep levels, frontal fold axes formed above the velocity discontinuity in a transfer zone deviated to become nearly parallel to the bulk shortening direction (Fig. 8). Several large folds parallel to the shortening direction are interpreted to have formed above an offset accommodation zone at the northern margin of the inverted graben of the High Atlas Mountains (Beauchamp, 2004). These folds are likely related to the thrusting of synrift rocks over a prior accommodation zone formed during the rifting. Deviations in the structural strike of fold axes and fault surfaces within transfer zones are also known in the Appalachian thrust belt (Bayona et al., 2003). Translation of the Palaeozoic allochthon over a ramp caused deflection of the tectonic transport trajectory, major cross folding, and rotation of earlier structures in the southern Appalachians (Tull and Holm, 2005).

4.4. Implications

The inversion of synrift normal faults is favourable for trapping hydrocarbons. From the example of the Atlas Mountains, it was suggested that hydrocarbons trapped in the original rift structures may have re-migrated toward the margins of the orogen upon the inversion of the rift system (Beauchamp et al., 1999). Transfer zones and relay ramps such as those produced in our sandbox models may influence the process of hydrocarbon migration and trapping (Wheeler, 1980; Morley et al., 1990; Peacock and Sanderson, 1994; Coskun, 1997). Inverted rift basins are structurally complex and often difficult to interpret in seismic data. The models may help to unravel the structure and evolution of these systems, leading to improved hydrocarbon exploration assessments.

Transfer zones may also act as conduits for hydrothermal fluids and/or igneous intrusions in sedimentary basins during rifting or inversion (Etheridge et al., 1985 and as reviewed by Gartrell, 1993). Relay fault systems and transfer fault zones developed over basement structures have been interpreted as controlling a broad variety of mineralization types and styles, including Mississippi-Valley-type (MVT) deposits (e.g. Great Basin, USA; Clendenin and Duane, 1990), sedimentary nickel, zinc and platinum group mineralization (e.g. Nick Basin, Yukon, Canada; Hulbert et al., 1992), diamond-bearing kimberlites and lamproites (White et al., 1995), and epithermal gold (e.g. Drummond Basin, Australia; Henley and Adams, 1992). Hydrothermal fluid flow in transfer zones developed over basement faults may also be associated with reservoir formation due to hydrothermal dolomitization (Davies and Smith, 2006). In illustrating the resultant geometry of structures developed during inversion of relay or transfer fault zones developed above basement faults during rifting our models may aid in the prediction of potentially prospective areas for mineral and petroleum exploration in sedimentary basins and fold and thrust belts.

5. Conclusions

CT-scanning of analogue models permitted a clear observation of the progressive development, reactivation and superposition of structures during extension and subsequent co-axial shortening. CT scans especially highlighted the reverse reactivation of steep normal faults during graben inversion. Variations in thickness or rheology of ductile layers, pre-existing frontal ramps or prescribed cuts in the strong ductile basal multilayer were seen to control the localisation and geometry of rift-bounding normal faults in the overlying sand layers, resulting in the formation of symmetrical or asymmetrical rifts. Propagation and overlapping rift culminations occurred in transfer zones of models during extension. Deviation of frontal fold axes in ductile layers, and deflection of frontal thrusts in sand layers were observed in inverted transfer zones during shortening. No new

connecting fault was formed in models in transfer zones. During inversion, steep rift-bounding normal faults were initially reactivated as reverse faults at the same steep dip angles (58–67°); with progressive shortening (after 100% inversion) faults rotated to increasingly flatter dips (19–38°). New thrust faults that formed outside inverted graben structures were flatter (20–34°) than reactivated normal faults. During inversion, the layers filling the rifts underwent lateral compression at depth. Marker sand layers in inverted grabens demonstrate fold-like structures and tilting in the rift and on the rift margins. Graben fill was pushed up and outwards creating local extension near the surface. Late superficial extension was expressed as local normal faulting at the top of models after 200% inversion.

The results of physical modelling provide a better understanding of the possible causes of differences in the orientation of structures during graben inversion. Modelling suggests that basement structures may affect the structural geometry of orogenic fronts in fold–thrust belts, influencing the evolution of sedimentary basins during the opening stage and resulting in different styles and orientation of structures during basin closure. Results may therefore aid the localisation of transverse basement faults that may have important implications in petroleum and mineral exploration.

Acknowledgements

We are grateful to the Editor Mike Sandiford and two anonymous reviewers for helpful suggestions and corrections that permitted to improve the manuscript considerably. Thanks are also due to the Donors of the American Chemical Society Petroleum Research Fund and to the Natural Sciences and Engineering Research Council of Canada (NSERC) for supporting this research through AC and Discovery grants respectively to L. Harris. Research was undertaken in the new INRS-ETE facility for physical, numerical and geophysical simulations funded by the Canadian Foundation for Innovation with contributions from the Ministère de l'Éducation, du Loisir et du Sport (Québec), INRS-ETE, the Applied Geodynamics Laboratory of the University of Texas at Austin, LaVision Inc., Sun Microsystems, NORSAR and Seismic Microtechnology. This work is partially supported by projects RFBR 05-05-65052, Scientific school-9664.2006.5. J. Labrie and S. Montreuil (INRS-ETE) operated the CT scanner. Thanks are due to S. Daniel (U. Laval) for assisting J. Poulin in image processing, M. Duchesne (GSC) and N. Pinet (CGC Quebec) for constructive review and discussion of modelling results, S. Castonguay (CGC Quebec) for a detailed review of an earlier draft, and M. Bousmina and M. Rousseau (U. Laval) for allowing equipment use and providing instruction in rheology measurements. PDMS was kindly provided by A. Cruden (U. Toronto). We are very grateful to *Tectonophysics* and *Elsevier Limited* for the permission that was granted to reproduce the seismic profiles from Letouzey et al. (1990) in our paper.

References

Acocella, V., Faccenna, C., Funiciello, R., Rossetti, F., 1999. Sand-box modelling of basement-controlled transfer zones in extensional domains. Terra Nova 11, 149–156.

Bayona, G., Thomas, W.A., Van der Voo, R., 2003. Kinematics of thrust sheets within transverse zones: a structural and paleomagnetic investigation in the Appalachian thrust belt of Georgia and Alabama. J. Struct. Geol. 25, 1193–1212.

Beauchamp, W., 2004. Superposed folding resulting from inversion of a synrift accommodation zone, Atlas Mountains, Morocco. In: McClay, K.R. (Ed.), Thrust tectonics and hydrocarbon systems. AAPG Memoir, vol. 82, pp. 635–646.

Beauchamp, W., Barazangi, M., Demnati, A., El Alji, M., 1996. Intracontinental rifting and inversion: Missour Basin and Atlas Mountains, Morocco. AAPG Bull. 80, 1459–1482.

Beauchamp, W., Allmendinger, R., Barazangi, M., Demnati, A., El Alji, M., Dahmani, M., 1999. Inversion tectonics and the evolution of the High Atlas Mountains, Morocco, based on a geological–geophysical transect. Tectonics 18, 163–184.

Brun, J.-P., Nalpas, T., 1996. Graben inversion in nature and experiments. Tectonics 15, 677–687.

Buchanan, P.G., McClay, K.R., 1991. Sandbox experiments of inverted listric and planar fault systems. Tectonophysics 188, 97–115.

Byerlee, J.D., 1968. Brittle–ductile transition in rocks. J. Geophys. Res. 96, 20161–20178.

Byrne, D., Harris, L.B., 1992. Fault patterns during normal and oblique rifting and the influence of basement discontinuities: application to models for the tectonic evolution of the Perth Basin, Western Australia. In: Rickard, M.J., et al. (Eds.), Basement Tectonics, vol. 9. Kluwer Academic Press, pp. 23–42.

Calassou, S., Larroque, C., Malavieille, J., 1993. Transfer zones of deformation in thrust wedges: an experimental study. Tectonophysics 221, 325–344.

Chandler, V.W., McSwiggen, P.L., Morey, G.B., Hinze, W.J., Anderson, R.R., 1989. Interpretation of seismic reflection, gravity and magnetic data across Middle Proterozoic Mid-Continent rift system, Northwestern Wisconsin, Eastern Minnesota and Central Iowa. AAPG Bull. 73, 261–275.

Childs, C., Watterson, J., Walsh, J.J., 1995. Fault overlap zones within developing normal fault systems. J. Geol. Soc. 152, 535–549.

Clendenin, C.W., Duane, M.J., 1990. Focused fluid flow and Ozark Mississippi Valley-type deposits. Geology 18, 116–119.

Cooke, A., Harris, L.B., 1987. Analogue modelling experiments during normal and oblique extension. Applied extension tectonics. Aust. BMR Rec. 51, 116–124.

Corfield, S., Sharp, I.R., 2000. Structural style and stratigraphic architecture of fault propagation folding in extensional settings: a seismic example from the Smørbukk area, Halten Terrace, Mid-Norway. Basin Res. 12, 329–341.

Coskun, B., 1997. Oil and gas fields-transfer zone relationships, Thrace basin, NW Turkey. Mar. Pet. Geol. 14, 401–416.

Cowie, P.A., Gupta, S., Dawers, N.H., 2000. Implications of fault array evolution for synrift depocentre development: insights from a numerical fault growth model. Basin Res. 12, 241–261.

Davies, G.R., Smith Jr., L.B., 2006. Structurally controlled hydrothermal dolomite reservoir facies: an overview. AAPG Bull. 90, 1641–1690.

Davy, P., Cobbold, P.R., 1991. Experiments on shortening of 4-layer continental lithosphere. Tectonophysics 188, 1–25.

Doré, A.G., Lundin, E.R., Fichler, C., Olesen, O., 1997. Patterns of basement structure and reactivation along the NE Atlantic margin. J. Geol. Soc. 154, 85–92.

Dubois, A., Odonne, F., Massonnat, G., Lebourg, T., Fabre, R., 2002. Analogue modelling of fault reactivation: tectonic inversion and oblique remobilisation of grabens. J. Struct. Geol. 24, 1741–1752.

Eisenstadt, G., Withjack, M.O., 1995. In: Buchanan, J.G., Buchanan, P.G. (Eds.), Estimating inversion: results from clay models. Basin Inversion: Geol. Soc. Lond. Spec. Pub., vol. 88, pp. 119–136.

Etheridge, M.A., 1986. On the reactivation of extensional fault systems. Philosophical Transactions of the Royal Society of London. Series A, Mathematical and Physical Sciences 317(1539). Major Crustal Lineaments and Their Influence on the Geological History of Continental Lithosphere, pp. 179–194.

Etheridge, M.A., Branson, J.C., Smith, P.G.S., 1985. Extensional basin-forming structures in Bass Strait and their importance for hydrocarbon exploration. APPEA J. 25, 344–361.

Gartrell, A.P., 1997. Evolution of rift basins and low-angle detachments in multilayer analogue extension experiments. Geology 25, 615–618.

Gartrell, A.P., 1993. Analogue modelling of transfer zones between offset rotational normal faults: implications for hydrocarbon and base metal exploration. Honours Thesis, The University of Western Australia (unpub.).

Gartrell, A.P., 2001. Crustal rheology and its effect on rift basin styles. Geol. Soc. Am. Mem. 193, 221–233.

Gartrell, A.P., Hudson, C., Evans, B., 2005. The influence of basement faults during extension and oblique inversion of the Makassar Straits rift system: insights from analog models. AAPG Bull. 89, 495–506.

Gawthorpe, R.L., Leeder, M.R., 2000. Tectono-sedimentary evolution of active extensional basins. Basin Res. 12, 195–218.

Gomez, F., Beauchamp, W., Barazangi, M., 2000. Role of the Atlas Mountains (northwest Africa) within the African–Eurasian plate-boundary zone. Geology 28, 775–778.

Harris, L.B., Higgins, R., Dentith, M.C., Middleton, M., 1994. Analogue modelling of transtensional faulting applied to the structure of the Perth Basin, Western Australia. In: Purcell, P.G., R.R. (Eds.), The Sedimentary Basins of Western Australia. Proc. Petrol. Expl. Soc. Aust. Symposium, Perth, pp. 801–810.

Hayward, N., Ebinger, C.J., 1996. Variations in the along-axis segmentation of the Afar rift system. Tectonics 15, 244–257.

Henley, R.W., Adams, D.P.M., 1992. Strike-slip fault reactivation as a control on epithermal vein-style gold mineralization. Geology 20, 443–446.

Higgins, R.I., Harris, L.B., 1997. The effect of cover composition on extensional faulting above reactivated basement faults: results from analogue modelling. J. Struct. Geol. 19, 89–98.

Hill, K.C, Keetley, J.T., Kendrick, R.D., Sutriyono, E., 2004. Structure and hydrocarbon potential of the New Guinea fold belt. In: McClay, K.R. (Ed.), Thrust tectonics and hydrocarbon systems. AAPG Mem., vol. 82, pp. 494–514.

Holdsworth, R.E., Butler, C.A., Roberts, A.M., 1997. The recognition of reactivation during continental deformation. J. Geol. Soc. 154, 73–78.

Hubbert, K.M., 1937. Theory of scale models as applied to the study of geologic structures. Geol. Soc. Amer. Bull. 48, 1459–1520.

Hulbert, L.J., Grégoire, D.C., Paktunc, D., Carne, R.C., 1992. Sedimentary nickel, zinc and platinum-group-element mineralisation in Devonian black shales at the Nick Property, Yukon, Canada: a new deposit style. Expl. Mining Geol. 1, 39–62.

Hus, R., Acocella, V., Funiciello, R., de Batist, M., 2005. Sandbox models of relay ramp structure and evolution. J. Struct. Geol. 27, 459–473.

Kirby, S.H., 1983. Rheology of the lithosphere. Rev. Geophys. Space Phys. 21, 1458–1487.

Koopman, A., Speksnijder, A., Horsfield, W.T., 1987. Sandbox model studies of inversion tectonics. Tectonophysics 137, 379–388.

Larsen, P., 1988. Relay structures in a Lower Permian basement involved extension system, East Greenland. J. Struct. Geol. 10, 3–8.

Le Calvez, J.H., Vendeville, B.C., 2002. Experimental designs to model along-strike fault interaction. J. Virt. Expl. 7, 7–23.

Letouzey, J., Werner, P., Marty, A., 1990. Fault reactivation and structural inversion. Backarc and intraplate compressive deformations. Example of the eastern Sunda shelf (Indonesia). Tectonophysics 183, 341–362.

Mandal, N., Chattopadhyay, A., 1995. Modes of reverse reactivation of domino-type normal faults: experimental and theoretical approach. J. Struct. Geol. 17, 1151–1163.

Mandl, G., 2000. Faulting in Brittle Rocks: an Introduction to the Mechanics of Tectonic Faults. Springer-Verlag, Berlin. 434 pp.

McClay, K.R., 1989. Analogue models of inversion tectonics. In: Cooper, M.A., Williams, G.D. (Eds.), Inversion Tectonics. Blackwell Scientific Publications, Oxford. Spec. Publ. Geol. Soc. London, vol. 44, pp. 41–59.

McClay, K.R., Dooley, T., Whitehouse, P., Mills, M., 2002. 4-D evolution of rift systems: Insights from scaled physical models. AAPG Bull. 86, 935–959.

McLeod, A., Dawers, N.H., Underhill, J.R., 2000. The propagation and linkage of normal faults: insights from the Strathspey–Brent–Stratfjord fault array, northern North Sea. Basin Res. 12, 263–284.

Michon, L., Sokoutis, D., 2005. Interaction between structural inheritance and extension direction during graben and depocentre formation: an experimental approach. Tectonophysics 409, 125–146.

Mitra, S., 1993. Geometry and kinematic evolution of inversion structures. AAPG Bull. 77, 1159–1191.

Morley, C.K., Wonganan, N., 2000. Normal fault displacement characteristics, with particular reference to synthetic transfer zones, Mae Moh mine, northern Thailand. Basin Res. 12, 307–327.

Morley, C.K., Nelson, R.A., Patton, T.L., Munn, S.G., 1990. Transfer zones in the East African Rift System and their relevance to hydrocarbon exploration in rifts. AAPG Bull. 74, 1234–1253.

O'Brien, G.W., Higgins, R., Symonds, P., Quaife, P., Colwell, J., Blevin, J., 1996. Basement control on the development of extensional systems in Australia's Timor Sea: an example of hybrid hard linked/soft linked faulting? APPEA J. 36, 161–201.

O'Brien, G.W., Morse, M., Wilson, D., Quaife, P., Colwell, J., Higgins, R., Foster, C.B., 1999. Margin-scale, basement-involved compartmentalisation of Australia's North West Shelf: a primary control on basin-scale rift, depositional and reactivation histories. APPEA J. 39, 40–61.

Ord, A., Hobbs, B.E., 1989. The strength of the continental crust, detachment zones and the development of plastic instabilities. Tectonophysics 158, 269–289.

Panien, M., Schreurs, G., Pfiffner, A., 2005. Sandbox experiments on basin inversion: testing the influence of basin orientation and basin fill. J. Struct. Geol. 27, 433–445.

Paton, D.A., Underhill, J.R., 2004. Role of crustal anisotropy in modifying the structural and sedimentological evolution of extensional basins: the Gamtoos Basin, South Africa. Basin Res. 16, 339–359.

Peacock, D.C.P., 2002. Propagation, interaction and linkage in normal fault systems. Earth Sci. Rev. 58, 121–142.

Peacock, D.C.P., Sanderson, D.J., 1994. Displacements, segment linkage and relay ramps in normal fault zones. AAPG Bull. 78, 147–165.

Poulin, J., Konstantinovskaya, E., Harris, L.B., 2006. Développement de méthodes et de techniques afin d'utiliser la tomodensitométrie en appui à la modélisation physique appliquée, la géologie structurale et la géomécanique. Geoscope 7, 13.

Ramberg, H., 1981. Gravity, Deformation and the Earth's Crust. Academic Press, London. 452 pp.

Schreurs, G., Hänni, R., Panien, M., Vock, P., 2003. Analysis of analogue models by helical X-ray computed tomography. Geol. Soc. London, Spec. Publ. 215, 213–223.

Sonder, L.J., England, P.C., 1986. Vertical averages of rheology of continental lithosphere: relation to thin sheet parameters. Earth Planet. Sci. Lett. 77, 81–90.

Tavarnelli, E., Butler, R.W.H., Decandia, F.A., Calamita, F., Grasso, M., Alvarez, W., Renda, P., 2004. Implications of fault reactivation and structural inheritance in the Cenozoic tectonic evolution of Italy. In: Crescenti, U., D'Offizi, S., Merlini, S., Sacchi, R. (Eds.), The Geology of Italy. Soc. Geol. Ital. Spec. Vol., pp. 201–214.

Tull, J.F., Holm, C.S., 2005. Structural evolution of a major Appalachian salient-recess junction: consequences of oblique collisional convergence across a continental margin transform fault. Geol. Soc. Amer. Bull. 117, 482–499.

Walsh, J.J., Childs, C., Meyer, V., Manzocchi, T., Imber, J., Nicol, A., Tuckwell, G., Bailey, W.R., Bonson, C.G., Watterson, J., Nell, P.A.R., Strand, J.A., 2001. Geometrical controls on the evolution of normal fault systems. In: Holdsworth, R.E., Strachan, R.A., Magloughlin, J.F., Knipe, R.J. (Eds.), The nature and tectonic significance of fault zone weakening. Geol. Soc. London, Spec. Publ., vol. 186, pp. 157–170.

Wheeler, R.L., 1980. Cross-strike structural discontinuities; possible exploration tool for natural gas in Appalachian Overthrust Belt. AAPG Bull. 64, 2166–2178.

White, S.H., de Boorder, H., Smith, C.B., 1995. Structural controls of kimberlite and lamproite emplacement. J. Geochem. Explor. 53, 245–264.

Wilson, R.W., McCaffrey, K.J.W., Holdsworth, R.E., Imber, J., Jones, R.R., Welbon, A.I.F., Roberts, D., 2006. Complex fault patterns, transtension and structural segmentation of the Lofoten Ridge, Norwegian margin: using digital mapping to link onshore and offshore geology. Tectonics 25, TC4018. doi:10.1029/2005TC001895.

Withjack, M.O., Olsen, P.E., Schlishe, R.W., 1995. Tectonic evolution of the Fundy rift basin, Canada: Evidence of extension and shortening during passive margin development. Tectonics 14, 390–405.

Yamada, Y., McClay, K.R., 2004. 3D analog modelling of inversion thrust structures. In: McClay, K.R. (Ed.), Thrust Tectonics and Hydrocarbon Systems. AAPG Mem., vol. 82, pp. 276–301.